Hull ML, Charnock-Jones DS, Chan CLK, Bruner-Tran KL, Osteen KG, Tom BDM, Fan TD and Smith SK (2003) Antiangiogenesis agents are effective inhibitors of endometriosis. J Clin Endocrin Metab 88,2889–2899.

Igarashi T, Konno R, Okamoto S, Moriya T, Sato S and Yajima A (2001) Involvement of granule-mediated apoptosis in the cyclic change of the normal human endometrium. Tohoku J Exp Med 193,13–25.

Irwin JC, Kirk D, King RJ, Quigley MM and Gwatkin RB (1989) Hormonal regulation of human endometrial stromal cells in culture: an in vitro model for decidualization. Fertil Steril 52,761–768.

Ito M, Hiramatsu H, Kobayashi K, Suzue K, Kawahata M, Hioki K, Ueyama Y, Koyanagi Y, Sugawara K, Tsuji K et al. (2002) NOD/SCID/g(c)(null) mouse: an excellent recipient mouse model for engraftment of human cells. Blood 100,3175–3182.

Jensen EV and Jacobson HI (1962) Basic guides to the mechanism of estrogen action. Recent Prog Horm Res 18,387.

King A, Wellings V, Gardner L and Loke YW (1989) Immunocytochemical characterization of the unusual large granular lymphocytes in human endometrium throughout in menstrual cycle. Hum Immunol 24,195–205.

Klentzeris LD, Bulmer JN, Warren A, Morrison L, Li TC and Cooke ID (1992) Endometrial lymphoid tissue in the timed endometrial biopsy: morphometric and immunohistochemical aspects. Am J Obstet Gynecol 167,667–674.

Kokawa K, Shikone T and Nakano R (1996) Apoptosis in the human uterine endometrium during the menstrual cycle. J Clin Endocrinol Metab 81,4144–4147.

Marbaix E, Kokorine I, Moulin P, Donnez J, Eeckhout Y and Courtoy PJ (1996) Menstrual breakdown of human endometrium can be mimicked in vitro and is selectively and reversibly blocked by inhibitors of matrix metalloproteinases. Proc Natl Acad Sci USA 93,9120–9125.

Markee JE (1940) Menstruation in intraocular endometrial transplants in the rhesus monkey. Contrib Embryol Carnegie Inst Wash 28,219–308.

McCune JM, Namikawa R, Kaneshima H, Shultz LD, Lieberman M and Weissman IL (1988) The SCID-hu mouse: murine model for the analysis of human hematolymphoid differentiation and function. Science 241,1632–1639.

Nelson S (1964) The Arterial Supply of the Uterus Adnexa of the Rhesus Monkey, Master's Essays. Johns Hopkins University, Baltimore, MD, USA.

Nisolle M, Casanas-Roux F and Donnez J (2000a) Early-stage endometriosis: adhesion and growth of human menstrual endometrium in nude mice. Fertil Steril 74,306–312.

Nisolle M, Casanas-Roux F, Marbaix E, Jadoul P and Donnez J (2000b) Transplantation of cultured explants of human endometrium into nude mice. Hum Reprod 15,572–577.

Noyes RW, Hertig AT and Rock J (1950) Dating the endometrial biopsy. Fertil Steril 1,3–25.

O'Mally BW, Sherman MR and Toft DO (1970) Progesterone 'receptors' in the cytoplasm and nucleus of chick oviduct target tissue. Proc Natl Acad Sci USA 67,501–508.

Rygaard J and Povlsen CO (1969) Heterotransplantation of a human malignant tumour to 'nude' mice. Acta Path Microbiol Scand. Acta Path Microbiol Scand 77,758–760.

Sato Y, Terada Y, Utsunomiya H, Koyanagi Y, Ito M, Miyoshi I, Suzuki T, Sasano H, Murakami T, Yaegashi N et al. (2003) Immunohistochemical localization of steroidogenic enzymes in human follicle following xenotransplantation of human ovarian cortex into NOD-SCID mice. Mol Reprod Dev 65,67–72.

Sugawara J, Fukaya T, Murakami T, Yoshida H and Yajima A (1997) Hepatocyte growth factor stimulates proliferation, migration, and lumen formation of human endometrial epithelial cells in vitro. Biol Reprod 57,936–942.

Tabibzadeh S (1995) Signals and molecular pathways involved in apoptosis with special emphasis on human endometrium. Hum Reprod Update 1,303–323.

Tabibzadeh S, Miller S, Dodson WC and Satyaswaroop PG (1999) An experimental model for the endometriosis in athymic mice. Front Biosci 1,4–9.

Weissman A, Gotlieb L, Colgan T, Jurisicova A, Greenblatt EM and Casper RF (1999) Preliminary experience with subcutaneous human ovarian cortex transplantation in the NOD-SCID mouse. Biol Reprod 60,1462–1467.

Zaino RJ, Satyaswaroop PG and Mortel R (1985) Histologic response of normal human endometrium to steroid hormones in athymic mice. Hum Pathol 16,867–872.

Zamah NM, Dodson MG, Stephens LC, Buttram VC, Besch PK and Kaufman RH (1984) Transplantation of normal and ectopic human endometrial tissue into athymic nude mice. Am J Obstet Gynecol 149,591–597.

*Submitted on March 9, 2004; resubmitted on October 4, 2004; accepted on January 12, 2005*

AIDS RESEARCH AND HUMAN RETROVIRUSES
Volume 21, Number 4, 2005, pp. 325–330


# Sequence Note

# Phylogenetic Heterogeneity of new HTLV Type 1 Isolates from Southern India in Subgroup A

SADAYUKI OHKURA,[1] MASAHIRO YAMASHITA,[2] TAKAFUMI ISHIDA,[3] PALLA-GEORGE BABU,[4,†] YOSHIO KOYANAGI,[5] NAOKI YAMAMOTO,[6] TOMOYUKI MIURA,[1] and MASANORI HAYAMI[1]

## ABSTRACT

**Seven isolates of human T cell leukemia virus type 1 (HTLV-1) were taken in southern India and phylogenetically analyzed to gain new insights into the origin and dissemination of HTLV-1 in the subcontinent. The new Indian HTLV-1s were found to be members of subgroup A (Transcontinental subgroup) of the Cosmopolitan group. They formed three different clusters (South African/Caribbean, Middle Eastern, and East Asian clusters). These results demonstrate that Indian HTLV-1s are genetically heterogeneous and include the most divergent strain of subgroup A. On the basis of these results, we speculate that subgroup A HTLV-1s may have been present for thousands of years in India.**

HUMAN T CELL LEUKEMIA VIRUS type 1 (HTLV-1) is the causative agent of adult T cell leukemia (ATL) and HTLV-1-associated myelopathy/tropical spastic paraparesis (HAM/TSP).[1–3] HTLV-1 has unique geographic and ethnologic distribution patterns. It is endemic mainly in Melanesia, the Caribbean basin, sub-Saharan Africa, and southwestern Japan and is highly prevalent among certain ethnic populations including Jews in Iran, the Ainu in Japan, Aboriginals in Australia, and Native Americans. These sporadic infections are thought to be vestiges of various migrations of HTLV-1 carriers from endemic areas, although how this distribution was established is not clear.

Seroepidemiological surveys have shown sporadic HTLV-1 infections in India. In a previous phylogenetic study,[4] Indian HTLV-1s were found to belong to the phylogenetic group that includes the Middle Eastern HTLV-1 strains, suggesting a possible link between these two areas. However, from that work it was unclear whether Indian HTLV-1 strains are indeed the closest to Middle Eastern strains, because clear phylogenetic separation of HTLV-1 strains could not be accomplished on the basis of the protein-encoding regions (*gag*, *pol*, *env*, and *pX* genes) analyzed in the previous work. In contrast to analyses based on these regions, analysis of the long terminal repeats (LTR) region permits finer separation of taxa within the genotype that includes Indian and Middle Eastern HTLV-1s. Thus, to gain new insights into the origin and dissemination of HTLV-1 in India, we phylogenetically analyzed seven new HTLV-1s from southern India on the basis of the LTR region.

The prevalence of HTLV-1 in southern India was examined by serological assays. Sera were collected in three districts of southern India (Kerala, Andhra Pradesh, and Tamil Nadu), and were tested by a particle agglutination (PA) test (Serodia HTLV-1; Fujirebio, Tokyo, Japan). Reactive sera in the PA test were further confirmed by an immunofluorescence assay as described previously.[2] Three serum samples were collected from Dravidian speakers living in Andhra Pradesh in southern India (Table 1) and phylogenetically analyzed. In addition, we analyzed HTLV-1s of four reported seropositives (two from the

[1]Laboratory of Primate Model, Experimental Research Center for Infectious Diseases, Institute for Virus Research, Kyoto University, Kyoto 606-8507, Japan.
[2]Divisions of Human Biology and Basic Sciences, Fred Hutchinson Cancer Research Center, Seattle, Washington.
[3]Department of Biological Sciences, Graduate School of Science, University of Tokyo, Tokyo, Japan.
[4]Christian Medical College Hospital, Tamil Nadu, India.
[5]Laboratory of Viral Pathogenesis, Institute for Virus Research, Kyoto University, Kyoto, Japan.
[6]Department of Molecular Virology, School of Medicine, Tokyo Medical and Dental University, Tokyo, Japan.
[†]We are deeply saddened to report that Palla-George Babu died in a traffic accident.

TABLE 1. SEVEN HTLV-1s ISOLATED FROM SOUTHERN INDIA IN THIS STUDY

| *HTLV-1 isolate* | *Place* | *Age (years)* | *Sex* | *Disease* | *Subject* | | | *Notes* |
|---|---|---|---|---|---|---|---|---|
| | | | | | *PA*[a] | *Western blot* | *IFA* | |
| AP15 | Andhra Pradesh | 60s | M | Nervous disease | NI | NI | NI | Inhabits inland near the Tamil Nadu district |
| IND001 | Andhra Pradesh | NI | F | NI | + | NI | NI | |
| IND002 | Andhra Pradesh | 11 | NI | NI | NI | NI | NI | Blood sample on filter paper |
| IN2 | Kerala | 47 | F | NI | NI | NI | NI | Wife of the subject from whom IN3 was isolated |
| IN3 | Kerala | 52 | M | ATL | +(16) | + | + | A migrant worker in the Middle East |
| Ma1 | Tamil Nadu | 20 | F | ARC | +(8192) | Not done | + | Also positive for HIV-1 |
| TNA | Tamil Nadu | 43 | F | NI | +(512) | NI | NI | Also positive for HIV-1 |

*Abbreviations:* ARC, AIDS-related complex; ATL, adult T cell leukemia; IFA, immunofluorescence assay; NI, no information available; PA, particle agglutination test.
[a]Figures in parentheses represent the titer of HTLV-1 antibodies.

Tamil Nadu district[5] and the other two from the Kerala district[6]) (Table 1). The two seropositives from Kerala were also Dravidian speakers. Two of the three Andhra Pradesh subjects (from whom IND001 and IND002 were isolated) said that they had had blood transfusions. It is unknown whether the other five subjects had received blood transfusions. Of the two Tamil Nadu subjects, the one from whom TNA was isolated was a commercial sexual worker and the one from whom Mal was isolated had sexual contacts with prostitutes.

For all but one of the subjects, chromosomal DNA (containing HTLV-1 proviral DNA) was extracted from either cultured or uncultured peripheral blood mononuclear cells (PBMCs) by a standard procedure with proteinase K. For the subject from whom IND002 was isolated, chromosomal DNA was extracted from whole blood that was blotted onto filter paper.[4] Randomly selected regions (approximately 1 $cm^2$) of the filter paper were cut into more than 100 pieces with sterile scissors. The pieces were put into 3 ml of 0.85% NaCl solution and shaken at room temperature for 1 hr. Supernatants were centrifuged for 1 min to precipitate free PBMCs, which were utilized for the subsequent extraction of DNA.

The extracted DNA was subjected to nested polymerase chain reaction (PCR) to amplify a part of the LTR region that corresponds to nucleotide positions 99 to 685 of ATK, a prototypic Japanese HTLV-1 strain, with special care to avoid cross-contamination of the amplified products as described previously.[7] Throughout this study, all negative controls gave negative signals. Nucleotide sequences of a part of the amplified LTR fragments that correspond to positions 122 to 628 of ATK were determined in both directions, using an automated DNA sequencer (Applied Biosystems, Foster City, CA). Nucleotide sequences were aligned with the computer software CLUSTAL W with minor manual modifications. Phylogenetic trees were constructed by the neighbor-joining (NJ) method. For construction of NJ trees, bootstrapping was done to generate 1000 resamplings of the original sequence alignments, and pairwise genetic distances were estimated on each resampling by the Kimura two-parameter method. Phylogenetic trees were then constructed with CLUSTAL W and the trees were visualized by TREEVIEW. Detailed procedures and references for construction of the trees are described elsewhere.[7] The GenBank accession numbers for the new strains are AY607576 to AY607582.

We amplified a part of the LTR region of seven new HTLV-1s from India (Table 1). HTLV-1 isolates are phylogenetically separated into three major genotypes. Most HTLV-1 isolates from the world form a large group called the Cosmopolitan group or HTLV-1a. HTLV-1 isolates from Central Africa and those from Melanesia have diverged from those of the Cosmopolitan group, and are thus collectively called the Central African (HTLV-1b and -1d) and Melanesian (HTLV-1c) groups, respectively. The LTR sequences of the newly isolated HTLV-1s exhibited higher genetic similarities to HTLV-1 strains of the Cosmopolitan group (97.1%) than to those of the Central African (94.4%) and Melanesian groups (91.3%). The phylogenetic analysis also placed the newly isolated HTLV-1s into the Cosmopolitan group (Fig. 1). This group has been divided into five subgroups (A to E) on the basis of their LTR sequences. Each of the five subgroups closely correlates with the geographic origins of its HTLV-1 isolates. According to our data (Fig. 1), all of the new HTLV-1 strains belong to subgroup A (Transcontinental subgroup). This was confirmed by their restriction fragment length polymorphism (RFLP) profiles, which are consistent with those of subgroup A in our classification. Namely, the analyzed LTR fragments of the new HTLV-1s have *Nde*I and *Sac*I sites, but not *Dra*I and *Mae*III sites, which is consistent with the RFLP patterns of subgroup A strains. All of these data demonstrate that the prevalent genotype of HTLV-1 in southern India is subgroup A of the Cosmopolitan group.

Because all of the new Indian isolates belong to subgroup A (Fig. 1), their nucleotide alignments were compared with those of subgroup A strains. The new strains formed three different clusters (Fig. 2). One cluster contained two of the new strains (IND001 and IND002) together with South African and Caribbean HTLV-1s (Caribbean/South African/Indian cluster). Another cluster contained two other Indian HTLV-1s (AP15 and TNA) together with mostly Middle Eastern HTLV-1s (Middle Eastern cluster). The third cluster contained the other three Indian isolates (IN2, IN3, and Mal) together with Japanese HTLV-1 strains. We tentatively refer to this cluster as the East Asian cluster. These clusters had the following characteristic nucleotide substitutions: HTLV-1s of the Caribbean/South African/Indian cluster have a G-to-A substitution at nucleotide position 246 in ATK, a C-to-T substitution at position 386, and an A-to-G substitution at position 575. Two of the Indian isolates (AP5 and TNA), like strains of the Middle Eastern cluster, have G rather than A at 240. It is noteworthy that within subgroup A, AP15 and TNA were phylogenetically located at the nodes of the Middle Eastern cluster, while Mal was branched off at the node of the East Asian cluster (Fig. 2). Collectively, these results indicate that subgroup A HTLV-1s circulating in India are polyphyletic.

The finding that HTLV-1s in southern India formed three different clusters indicates that the HTLV-1s of southern India are highly heterogeneous. This heterogeneity is in sharp contrast to the homogeneity of subgroup A HTLV-1s from other geographic areas. For example, HTLV-1s of South America and the Middle East form respective clusters (the Latin American and Middle Eastern clusters) within subgroup A. In addition, as shown in Fig. 1, India has the most divergent strain of subgroup A (SG).[8,9] The present analysis further showed that within subgroup A, some of the new Indian HTLV-1s are phylogenetically located at or branched off the node of the Middle Eastern and East Asian clusters. As a result, subgroup A HTLV-1s in southern India are clearly distinguishable from those of other geographic areas in that southern India has both the most divergent HTLV-1 and highly heterogeneous HTLV-1s.

These findings have an interesting implication with respect to the origin of HTLV-1 in India. Earlier studies hypothesized that HTLV-1 was introduced into India by recently migrated peoples such as African slaves several hundreds years ago, or by Jewish populations that migrated from the Middle East about 1000 to 1300 years ago.[4] However, our results indicate that Indian HTLV-1 is much more heterogeneous and includes more divergent strains than subgroup A HTLV-1 of other geographic origins such as Africa and the Middle East. This implies that HTLV-1 has been present in India for much longer than 1300 years.

If this is correct, how did HTLV-1 get to India? HTLV-1 isolates analyzed in the present study were isolated from the Dravidians, a population that migrated to India several thousand years ago. The high heterogeneity and divergence of HTLV-1 in southern India may be explained by the genetic vari-

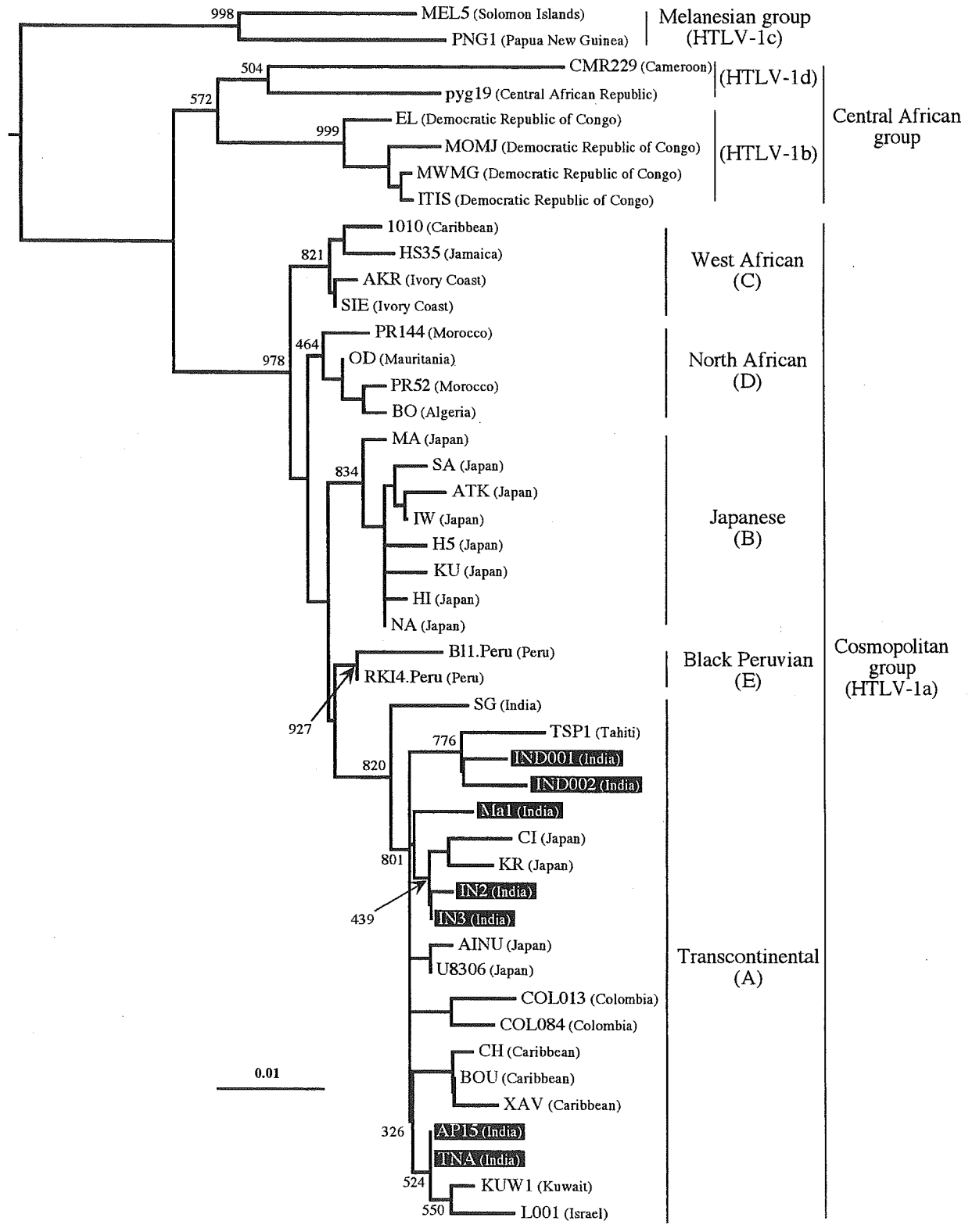


**FIG. 1.** Phylogenetic tree of HTLV-1 isolates based on a part of the LTR region (nucleotide positions 122–628 in ATK), showing the evolutionary relationships between the new isolates from India and isolates previously reported. Newly isolated HTLV-1s from India are highlighted. The tree was constructed by using the neighbor-joining (NJ) method. The scale at the bottom of the tree indicates the number of nucleotide substitutions per site. The horizontal branch lengths are proportional to the genetic distance. Numbers at nodes are bootstrap values. The tree was rooted with a prototype isolate of HTLV-2, MoT. The other DNA sequences used for construction of the phylogenetic tree have been described previously.[7]

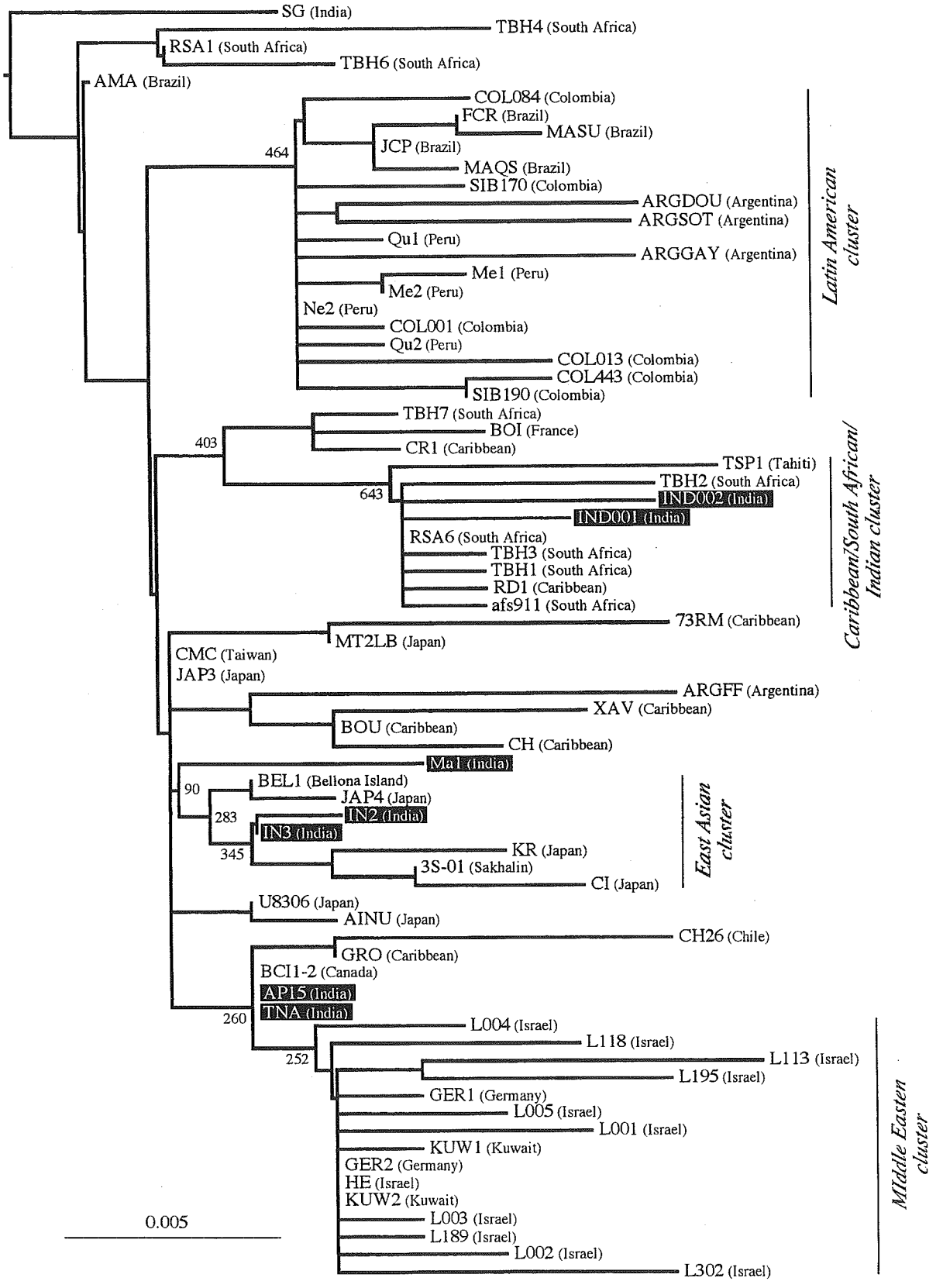


**FIG. 2.** Phylogenetic tree of HTLV-1 isolates that belong to subgroup A. The new isolates from India are boxed in black. The tree was constructed on the basis of a part of the LTR region (nucleotide positions 122–628 in ATK) by using the NJ method. The tree was rooted with strains of the Central African and Melanesian groups. For details, see the legend to Fig. 1.

ability of populations in the southern parts of India, where the Dravidians are the major inhabitants and HTLV-1 is highly prevalent.[10–12] The genetic diversity of the southern Indian populations was estimated to be as high as that of Africans and even higher than that of Europeans and other Asians based on sequence data of mitochondrial DNA and the allele frequency of several genetic loci.[13] Taken together, these findings imply that different lineages of the Dravidians carried different genotypes of subgroup A HTLV-1 when they reached India.

According to this scenario, some of the HTLV-1s in India could have been taken to other HTLV-1-prevalent areas such as the Middle East, South Africa, and the Caribbean basin. The genetic similarities between two of the new Indian isolates (AP15 and TNA) and the Middle Eastern isolates (Fig. 2), as well as the geographic proximity of India and the Middle East, strongly suggest movements of HTLV-1 carriers between these two areas, which is consistent with previous reports.[4] If this is the case, HTLV-1 might have been brought from India to the Middle East on the basis of the higher diversity among HTLV-1s in southern India than among Middle Eastern HTLV-1s (Fig. 2). Our results also show that two of the new isolates (IND001 and IND002) were phylogenetically related to South African and Caribbean HTLV-1s. This raises the possibility that some Indian HTLV-1s were introduced to South Africa and the Caribbean basin, as was previously proposed.[14] This possibility is consistent with the facts that more than a half million Indians migrated to the Caribbean basin as indentured laborers after the abolition of the trans-Atlantic slave trade in the early nineteenth century, and that South Africa served as a waystation during the migration.

After the putative introduction of Indian HTLV-1 to South Africa, some of the migrants may have gone back to India, possibly carrying human immunodeficiency virus type 1 (HIV-1). This is because the seropositivity against HTLV-1 among HIV-1 seropositives was significantly higher than that among HIV seronegatives in southern India.[11] This suggests that HTLV-1 was sexually transmitted among some HIV-1 seropositives in southern India. As Indian HIV likely originated from South Africa, some Indian HTLV-1s may have originated from the same place.

In summary, we speculate that Dravidian speakers originally carried HTLV-1 to southern India. This is supported by the following two points. First, the seven HTLV-1s isolated in southern India in this study are all in subgroup A and are highly heterogeneous. Second, India has the most divergent strain of subgroup A[9] (Fig. 1). Nonetheless, it is unclear how Dravidian speakers originally acquired HTLV-1. With respect to the origin of HTLV-1 of the Dravidians, it is interesting that the sickle cell gene haplotypes in southern India are the same as those in Africa,[15] and that the Dravidian languages have some similarities to those spoken in the Sahel Belt of Africa (from Sudan to Senegal).[16] It also remains unclear why HTLV-1s of Japan and South America are phylogenetically related to those of India. Future phylogenetic analyses of HTLV-1s in the Sahel Belt and South and Central Asia will help to identify the origin of Indian HTLV-1 and elucidate how it was disseminated in Asia.

## ACKNOWLEDGMENT

This work was supported by a Grant-in-Aid from the Ministry of Education, Science, Sports, and Culture, Japan.

## REFERENCES

1. Gessain A, Barin F, Vernant J, *et al.*: Antibodies to human T-lymphotropic virus type-I in patients with tropical spastic paraparesis. Lancet 1985;ii:407–409.
2. Hinuma Y, Nagata K, Hanaoka M, *et al.*: Adult T-cell leukemia: Antigen in an ATL cell line and detection of antibodies to the antigen in human sera. Proc Natl Acad Sci USA 1981;78:6476–6480.
3. Poiesz B, Ruscetti F, Gazdar A, *et al.*: Detection and isolation of type C retrovirus particles from fresh and cultured lymphocytes of a patient with cutaneous T-cell lymphoma. Proc Natl Acad Sci USA 1980;77:7415–7419.
4. Nerurkar V, Babe P, Song K, *et al.*: Sequence analysis of human T cell lymphotropic virus type I strains from southern India: Gene amplification and direct sequencing from whole blood blotted onto filter paper. J Gen Virol 1993;74:2799–2805.
5. Koyanagi Y, Yoshida T, Suzuki M, *et al.*: Dual infection of HIV-1 and HTLV-I in south India: A study on a patient with AIDS-related complex. Microbiol Immunol 1993;37:983–986.
6. Chandy M, Babu P, Saraswathi N, Ishida T, and John T: HTLV-I infection in patients with leukaemia in southern India. Lancet 1991;338:380–381.
7. Ohkura S, Yamashita M, Cartier L, *et al.*: Identification and phylogenetic characterization of a human T-cell leukaemia virus type I isolate from a native inhabitant (Rapa Nui) of Easter Island. J Gen Virol 1999;80:1995–2001.
8. Hashimoto K, Lalkaka J, Fujisawa J, *et al.*: Limited sequence divergence of HTLV-I of Indian HAM/TSP patients from a prototype Japanese isolate. AIDS Res Hum Retroviruses 1993;9: 495–498.
9. Miura T, Fukunaga T, Igarashi T, *et al.*: Phylogenetic subtypes of human T-lymphotropic virus type I and their relations to anthropological background. Proc Natl Acad Sci USA 1994;91:1124–1127.
10. Roy M, Das MK, Ishida T, *et al.*: Absence of HTLV-I infection in some Indian populations. Indian J Med Res 1994;100:160–162.
11. Babu P, Ishida T, Nesadoss J, and John T: Prevalence of HTLV-I/II antibodies in HIV seropositive and HIV seronegative STD patients in Vellore region in southern India. Scand J Infect Dis 1995;27:105–108.
12. Kelkar R, Ishida T, Bharucha Z, Advani SH, and Hayami M: Seroepidemiological survey of HTLV-I in blood donors in India. Indian J Haematol 1990;8:11–14.
13. Majumder PP: People of India: Biological diversity and affinities. Evol Anthropol 1998;6:100–110.
14. Song K, Nerurkar V, Pereira-Cortez A, *et al.*: Sequence and phylogenetic analyses of human T cell lymphotropic virus type I from a Brazilian woman with adult T cell leukemia: Comparison with virus strains from South America and the Caribbean basin. Am J Trop Med Hyg 1995;52:101–108.
15. Niranjan Y, Chandak GR, Veerraju P, and Singh L: Some atypical and rare sickle cell gene haplotypes in populations of Andhra Pradesh, India. Hum Biol 1999;71:333–340.
16. Koenraad E: Some new arguments. In: *Update on the Aryan Invasion Debate*. Aditya Prakashan, Delhi, India, 1999, pp. 238–320.

Address reprint requests to:
*Masanori Hayami*
*Laboratory of Primate Model*
*Experimental Research Center for Infectious Diseases*
*Institute for Virus Research*
*Kyoto University*
*Kyoto 606-8507, Japan*

*E-mail:* mhayami@virus.kyoto-u.ac.jp

*J. Biochem.* **138**, 583–592 (2005)
doi:10.1093/jb/mvi158

# Solution RNA Structures of the HIV-1 Dimerization Initiation Site in the Kissing-Loop and Extended-Duplex Dimers

**Seiki Baba[1], Ken-ichi Takahashi[1,2], Satoko Noguchi[1], Hiroshi Takaku[1], Yoshio Koyanagi[3], Naoki Yamamoto[4] and Gota Kawai[1,*]**

*[1]Department of Life and Environmental Sciences, Chiba Institute of Technology, 2-17-1 Tsudanuma, Narashino, Chiba 275-0016; [2]Department of Bioscience, Faculty of Bioscience, Nagahama Institute of Bio-Science and Technology, 1266 Tamura-cho, Nagahama, Shiga 526-0829; [3]Institute for Virus Research, Kyoto University, Kyoto 606-8507; and [4]AIDS Research Center, The National Institute of Infectious Diseases, Toyama 1-23-1, Shinjuku-ku, Tokyo 162-8640*

Received April 27, 2005; accepted August 13, 2005

**Dimer formation of HIV-1 genomic RNA through its dimerization initiation site (DIS) is crucial to maintaining infectivity. Two types of dimers, the initially generated kissing-loop dimer and the subsequent product of the extended-duplex dimer, are formed in the stem-bulge-stem region with a loop including a self-complementary sequence. NMR chemical shift analysis of a 39mer RNA corresponding to DIS, DIS39, in the kissing-loop and extended-duplex dimers revealed that the three dimensional structures of the stem-bulge-stem region are extremely similar between the two types of dimers. Therefore, we designed two shorter RNA molecules, loop25 and bulge34, corresponding to the loop-stem region and the stem-bulge-stem region of DIS39, respectively. Based upon the chemical shift analysis, the conformation of the loop region of loop25 is identical to that of DIS39 for each of the two types of dimers. The conformation of bulge34 was also found to be the same as that of the corresponding region of DIS39. Thus, we determined the solution structures of loop25 in each of the two types of dimers as well as that of bulge34. Finally, the solution structures of DIS39 in the kissing-loop and extended-duplex dimers were determined by combining the parts of the structures. The solution structures of the two types of dimers were similar to each other in general with a difference found only in the A16 residue. The elucidation of the structures of DIS39 is important to understanding the molecular mechanism of the conformational dynamics of viral RNA molecules.**

**Key words: DIS, HIV-1, NMR, RNA, structure.**

Abbreviations: DIS, dimerization initiation site; HIV-1, human immunodeficiency virus type 1.

Two molecules of viral genomic RNA are packaged in a dimeric state in the virion of human immunodeficiency virus type 1 (HIV-1), and this dimer formation is crucial to maintaining their infectivity (*1–4*). Accumulating evidence from both *in vivo* and *in vitro* experiments has shown that the specific sequence, the dimerization initiation site (DIS) located close to the 5′ terminus of the genomic RNA, is required for spontaneous dimerization of HIV-1 RNA. DIS can form a stem-loop structure with a self-complementary sequence in the loop and a bulge in the stem (*5*, *6*). The dimerization of DIS forms the kissing-loop dimer as the first step; then, their intramolecular stems are converted into intermolecular stems, generating the extended-duplex dimer (*7*, *8*). This two step dimerization process is called the kissing-loop mechanism. The kissing-loop dimer is converted into the extended-duplex dimer by incubation at 55°C (*9*, *10*) or by incubation at physiological temperature with the HIV-1 nucleocapsid protein, NCp7, which includes two basic regions and two zinc-fingers (*11*). A number of experiments have been performed to gain an understanding of the role of the zinc-fingers as well as the basic regions (*12–16*). Our previous results show that, for the two step dimerization from the kissing-loop dimer to the extended-duplex dimer, the two basic regions surrounding the N-terminal zinc finger of NCp7 have RNA chaperone activity by themselves, and the zinc fingers increase the efficiency of the activity (*17*, *18*).

A number of three dimensional structural analyses using NMR and X-ray methods have been performed to determine the conformation of each region of DIS, the loop region in the kissing-loop (*19*, *20*) or extended-duplex dimers (*21–24*), as well as the bulge-out region (*25–27*). However, our previous studies suggested that the 39mer RNA sequence, DIS39, which covers the entire bulge and loop regions, is necessary and sufficient for the two step dimerization (*28*, *29*). Thus, it is still relevant to determine the structures of the kissing-loop and extended-duplex dimers for DIS39 with the same sequence and conditions.

In the present study, we designed two shorter RNA molecules, loop25 and bulge34; loop25 includes the loop-stem region of DIS39, and bulge34 includes the stem-bulge-stem region (Fig. 1), respectively we then determined the solution structures of loop25 in each of the kissing-loop and extended-duplex dimers as well as bulge34. By combining the structure parts, the solution structures of DIS39 in the kissing-loop and extended-duplex dimers were able to be determined.

*To whom correspondence should be addressed. Tel/Fax: +81-47-478-0425, E-mail: gkawai@sea.it-chiba.ac.jp

 

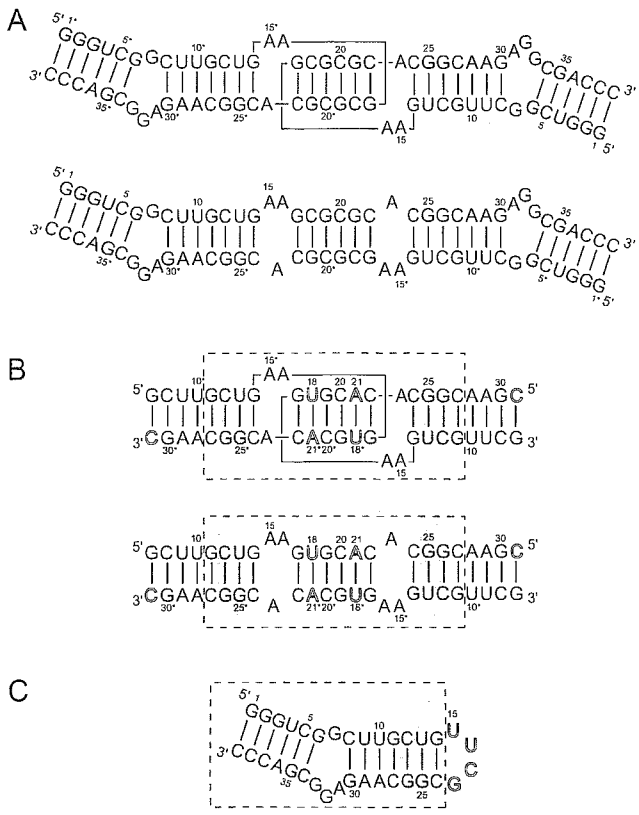

Fig. 1. **Secondary structure of a 39mer RNA corresponding to the dimerization initiation site (DIS39) and its fragments used in this study.** (A) The kissing-loop and extended-duplex dimers of DIS39. (B) The kissing-loop and extended-duplex dimers of loop25, which is composed of the loop and stem of DIS39. Modified residues are indicated by open characters. The sequence of the self-complementary loop was modified to increase the dispersion of NMR signals, and a base pair was added to the stem. The broken box indicates the part to be used for structure calculation. (C) Bulge34 consists of the stem-bulge-stem region of DIS39 and the connecting UUCG loop. The broken box indicates the part to be used for structure calculation. Gray shading indicates the two base pairs, C12–G26 and U13–G25, that are superimposed to combine the structures of the kissing-loop or extended-duplex dimer region and the stem-bulge-stem region. Asterisks indicate residues in the other strand.

## MATERIALS AND METHODS

*RNA Synthesis, Purification and Preparation*—Non-labeled loop25 was synthesized chemically by the phosphoramidite method with an automatic DNA/RNA synthesizer, Expedite model 8909 (PerSeptive Biosystems Inc., MA, USA). The protection groups were removed with ammonia and tetra-*n*-butylammonium fluoride. Non-labeled DIS39 and bulge34 were synthesized enzymatically by the *in vitro* transcription reaction method with AmpliScribe T7 transcription kits (Epicentre Technologies Co., WI, USA). Purification for each RNA sample was performed by PAGE using 30 cm × 40 cm glass plates (Nihon Eido Co. Ltd., Tokyo, Japan) under denaturing conditions, and extensive desalting by ultrafiltration (Centricon YM3, Amicon Inc., MA, USA) was carried out. For stable isotopic labeling by the *in vitro* transcription with $^{13}C$- and $^{15}N$-labeled NTPs (Nippon Sanso, Tokyo, Japan), we used DIS39 rather than shorter loop25 and bulge34 because the efficiency of *in vitro* transcription is better for larger RNA.

For the preparation of the kissing-loop dimer, DIS39 or loop25 in water was incubated at 368 K for 5 min and chilled on ice for 5 min. Then, the solvent was adjusted to 1× PN-buffer [10 mM sodium phosphate (pH 7.0) and 50 mM NaCl] by adding concentrated buffer. For the preparation of the extended-duplex dimer, DIS39 or loop25 in 1× PN-buffer was incubated at 368 K for 5 min and slowly cooled to room temperature. Bulge34 was annealed by heating at 363 K for 5 min and snap-cooling on ice. To confirm the formation of the hairpin structure, the samples were subjected to a native PAGE experiment. For NMR measurements, RNA samples were dissolved in 10 mM sodium phosphate buffer (pH 7.0) containing 50 mM NaCl. The final concentration of chemically synthesized loop25 was 1.8 mM. The concentrations of DIS39 and bulge34 (transcripts) were 1.0 and 0.5 mM, respectively. The concentration of the kissing-loop and extended-duplex dimers of [G-$^{13}C/^{15}N$] and [A-$^{13}C/^{15}N$] DIS39 were 0.4, 0.3, 0.2 and 0.1 mM, respectively.

*NMR Measurements*—NMR spectra were recorded on Bruker DRX-500 and DRX-600 spectrometers. Spectra were recorded at probe temperatures of 283 to 303 K and NMR data at 298 K were used for structure calculation. The imino proton signal of the G and U residues in $H_2O$ were distinguished from each other by the HSQC selected and HSQC filtered 1D spectra measured with $^{13}C$ and $^{15}N$-labeled DIS39. Exchangeable proton NOEs were determined by 2D NOESY in $H_2O$ with a mixing time of 150 ms using the jump-and-return scheme and gradient pulses for water suppression. For resonance assignments, well-established procedures were used (*30*). The H2 protons of adenosine were assigned based on a 2D HSQC experiment with natural abundance $^{13}C$. NOE distance restraints from non-exchangeable protons were obtained from 2D NOESY experiments (mixing times of 50, 100, 200, and 400 ms) in $D_2O$. The intensities of the NOEs between exchangeable protons were interpreted as distances of 2.1–5.0 Å. For loop25, distances were estimated by analyzing the initial slope of NOE intensities for mixing times of 25, 50, 100, 200 ms. Judgment of intermolecular NOE is described in the result section. Two restraints (>5 Å) were added to the distance restraints based on the absence of NOE cross peaks in the case of the kissing-loop dimer. For bulge34, the intensities of NOEs due to nonexchangeable protons were interpreted as distances with a margin of −1.5 to +1.5 Å for the 100 ms 2D NOESY and −1.0 to +2.0 Å for the 200 ms 2D NOESY. Two restraints (>5 Å) were added to the distance restraints based on the absence of NOE cross peaks. The formation of hydrogen binding of G:C, A:U or G:U base pairs is interpreted as distance constraints as 1.8–2.1 Å for hydrogen and acceptor atoms and 2.8–3.2 Å for donor and acceptor atoms; G11:C27 to G14:C24, G11*:C27* to G14*:C24* and G17:C22* to C22:G17* for loop25 in the kissing-loop dimer, G11:C27* to G14:C24*, G11*:C27 to G14*:C24 and G17:C22* to C22:G17* for loop25 in the extended-duplex dimer, and G1:C39 to C5:G35 and U9:A29 to G14:C24 for bulge34. Dihedral restraints were obtained as described below. The absence of crosspeaks between H1′–H2′ in the 2D TOCSY and DQF-COSY experiments was interpreted as the residue being in the C3′-*endo*

conformation. On the other hand, the presence of strong crosspeaks between H1′–H2′ in the 2D TOCSY and DQF-COSY experiments was interpreted as the residue being in the C2′-*endo* conformation. The correction of sugar puckering is interpreted as dihedral restraints for $\nu_2$ as 40.00 ± 20.00° (C3′-*endo*) or −35.00 ± 20.00° (C2′-*endo*). Based on the sequential connectivity of the Watson-Crick and G-U base pairs, the RNA-A conformation was assumed for the stem region and dihedral restraints were introduced for backbone torsion angles (α, β, γ, δ, ε and ζ) as the ideal conformation with a margin of ±10.00°. For loop25 in the kissing-loop dimer, information about the C3′-*endo* conformation (G11–G14, G17–C27), the C2′-*endo* conformation (A16) and RNA-A conformation in the stem region (G11–U13, U18–A21, G25–C27) was used as the dihedral restraints. For loop25 of the extended-duplex dimer, information about the C3′-*endo* conformation (G11–G14, G17-C27) and RNA-A conformation in the stem region (G11–U13, U18–A21, G25–C27) was used as the dihedral restraints. For bulge34, the information about the C3′-*endo* conformation (G1–G14, C24–A31, C34–C39) and RNA-A conformation in the stem region (G1–C5, G11–G14, C24–C27, G35–C39) was used as the dihedral restraints.

*Structure Calculation*—A set of 100 structures was calculated using the simulated annealing protocol described below with the InsightII/Discover package, and the amber force field was used. The force constants were 100 kcal $mol^{-1}$ $Å^{-2}$ for distance restraints and 100 kcal $mol^{-1}$ $rad^{-2}$ for dihedral restraints. The starting coordinates were randomized, and the randomized structures were heated to 2,000 K in 5 ps, and the temperature was kept to 2,000 K for another 5 ps. After that, all restraints were increased to full values in 20 ps, then, decreased to 1/10 of full values in 5 ps at 2,000 K. Van der Waals radii were increased from 0.1 to 0.825 in 20 ps at 2,000 K. All restraints were increased to full value again in 10 ps at 2,000 K. Scalings for non-bond interactions were increased to full value in the next 20 ps at 2,000 K, and the temperature was kept to 2,000 K for another 5 ps. Then, the temperature was gradually scaled to 300 K in 10 ps. After that, the structure was heated from 300 to 1,000 K in 5 ps, and the van der Waals radii were increased from 0.825 to 1 at 1,000 K, and then decreased from 1 to 0.825 at 1,000 K. An additional 5 ps of dynamics was performed at 1,000 K, and the temperature was gradually scaled to 300 K for 10 ps. A final minimization step was performed, which included a Lennard-Jones potential and electrostatic terms with a dielectric constant of 7. The ten final structures with the lowest total energies were chosen.

## RESULTS AND DISCUSSION

*Analysis of the NMR Spectra of DIS39, Loop25 and Bulge34*—Our previous NMR study revealed that the two types of dimers of DIS39 prepared as described in "MATERIALS AND METHODS" correspond to the kissing-loop and extended-duplex dimers (*31*). NMR spectra of DIS39 in each of the kissing-loop and extended-duplex dimers were measured in $D_2O$, and the signals due to H1′, H6/H8 were assigned by the sequential assignment method (Fig. 2). Figure 3A shows the difference in the chemical shift of H1′, H6/H8 between the two types of dimers. It was found that the difference is concentrated in the loop region. Interestingly, structures of the stem-bulge-stem region of the kissing-loop and extended-duplex dimers were extremely similar, even though the stems are formed by intra and inter molecules. This was also shown by analysis of the TOCSY spectrum; differences are located in the loop regions. Most residues were adapted to the C3′-*endo* conformation except for G32, G33 in the bulge-out region of both forms, A16 in the kissing-loop dimer and A15, A16 in the extended-duplex dimer, which might be a mixture of the C2′-*endo* and C3′-*endo* conformations.

To reveal further authentic structure, two RNA molecules were designed; loop25 includes the loop region and bulge34 includes the stem-bulge-stem region (Fig. 1, B and C). Loop25 was constructed to determine the authentic structure of the loop region. In order to increase the dispersion of the NMR signals, the sequence of the loop was modified from GCGCGC to GUGCAC. One base pair was added by replacing A31 by C31 in the stem to increase the stability of the kissing-loop dimer. It is noted that the loop sequences of GCGCGC and GUGCAC correspond to those of HIV-1 subtypes B and F (*32*), respectively, and both sequences have dimerization activity (*6*, *9*, *10*). The chemical shifts of loop25 were compared with those of DIS39 in each of the kissing-loop and extended-duplex dimers (Fig. 3, B and C). For both conformations, the chemical shifts for most of the stem region and A15, A16 and A23 were strikingly similar between the loop25 and DIS39. Due to the base alterations, the chemical shifts of the self complement loop were slightly different for both dimers. The chemical shift of H8 was shifted more than 0.2 ppm due to the addition of the terminal base pair. It is noteworthy that the chemical shift difference in loop25 between the kissing-loop and extended-duplex dimers (Fig. 3D) was almost identical to that of DIS39 (Fig. 3A). These results indicate that the structures of loop25 in the kissing-loop and extended-duplex dimers are essentially identical to those of DIS39. Upon analysis of the TOCSY spectrum, it was found that most of the residues were adapted to the C3′-*endo* conformation except A15 and A16 for the extended duplex dimer and A16 for the kissing loop dimer, and these results also agree with the results for DIS39.

Bulge34 was constructed to determine the authentic structure of the stem-bulge-stem region. Bulge34 consists of the stem-bulge-stem region of DIS39 and the connecting UUCG loop. The NMR signals of bulge34 were assigned by the sequential assignment technique. The chemical shift of H1′, H6/H8 of bulge34 were compared to those of DIS39 in the kissing-loop dimer (Fig. 3E). The chemical shifts for the stem-bulge-stem regions of bulge34 and DIS39 were identical, although the chemical shifts of the residues adjacent to the loop were slightly different by reflecting the difference in the closing loop sequences. Upon analysis of the TOCSY spectrum, it was found that most residues were adapted to the C3′-*endo* conformation except for G32, G33 in the bulge-out region and C in the UUCG loop, and that the conformation in the stem-bulge-stem region also agreed with that of DIS39. These results indicate that the structure of the stem-bulge-stem region of bulge34 is identical to that of DIS39.

Thus, the structures of DIS39 for two types of dimers can be determined by determining the structures of loop25 and bulge34, and combining them.

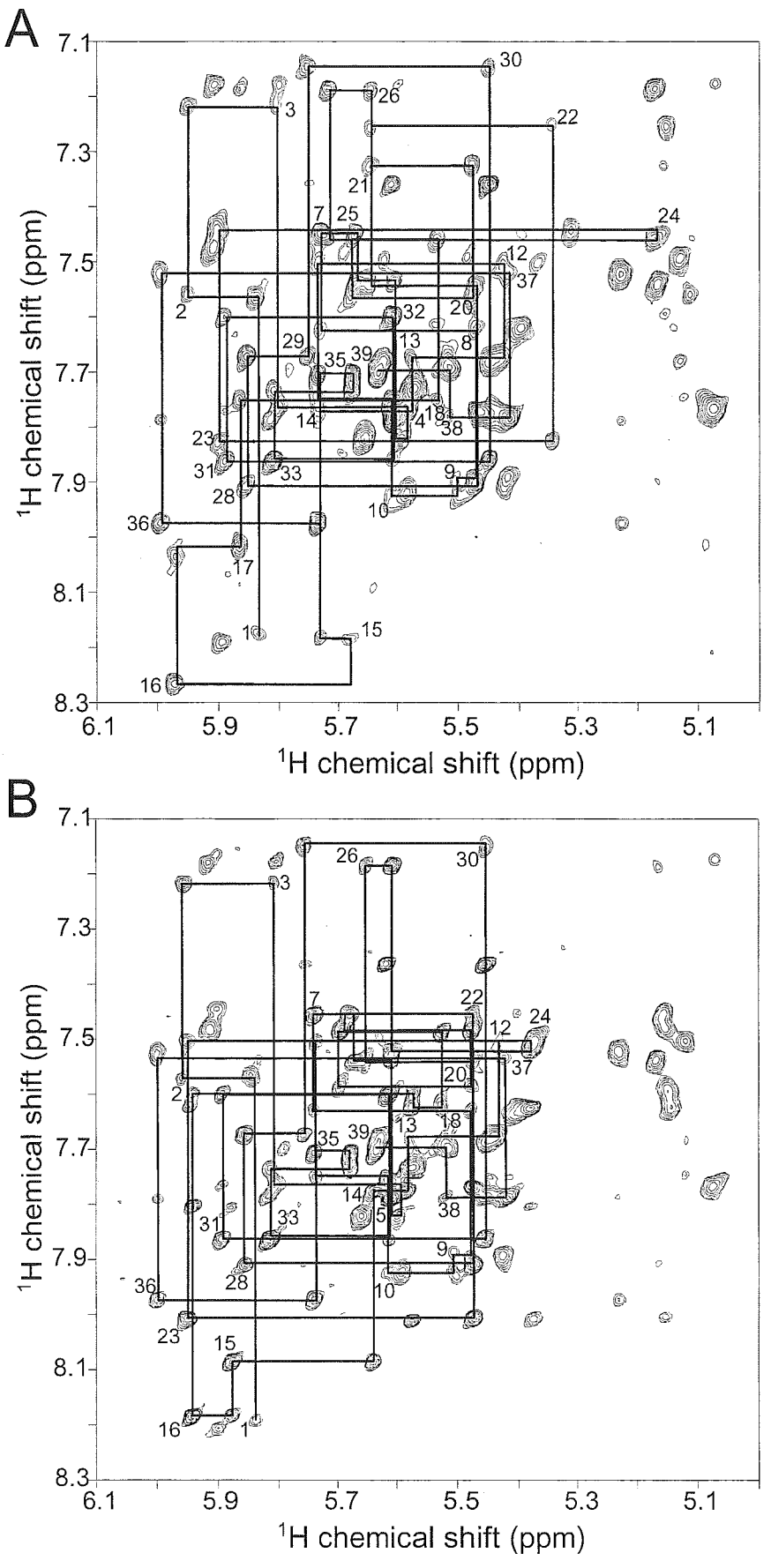


Fig. 2. **2D NOESY spectra of the (A) kissing-loop and (B) extended-duplex dimers of DIS39 measured in $D_2O$ at 25°C with a mixing time of 200 ms.** Cross-peaks between aromatic H6/H8 protons and ribose H1′ protons are shown, and the sequential NOE connectivity is indicated.

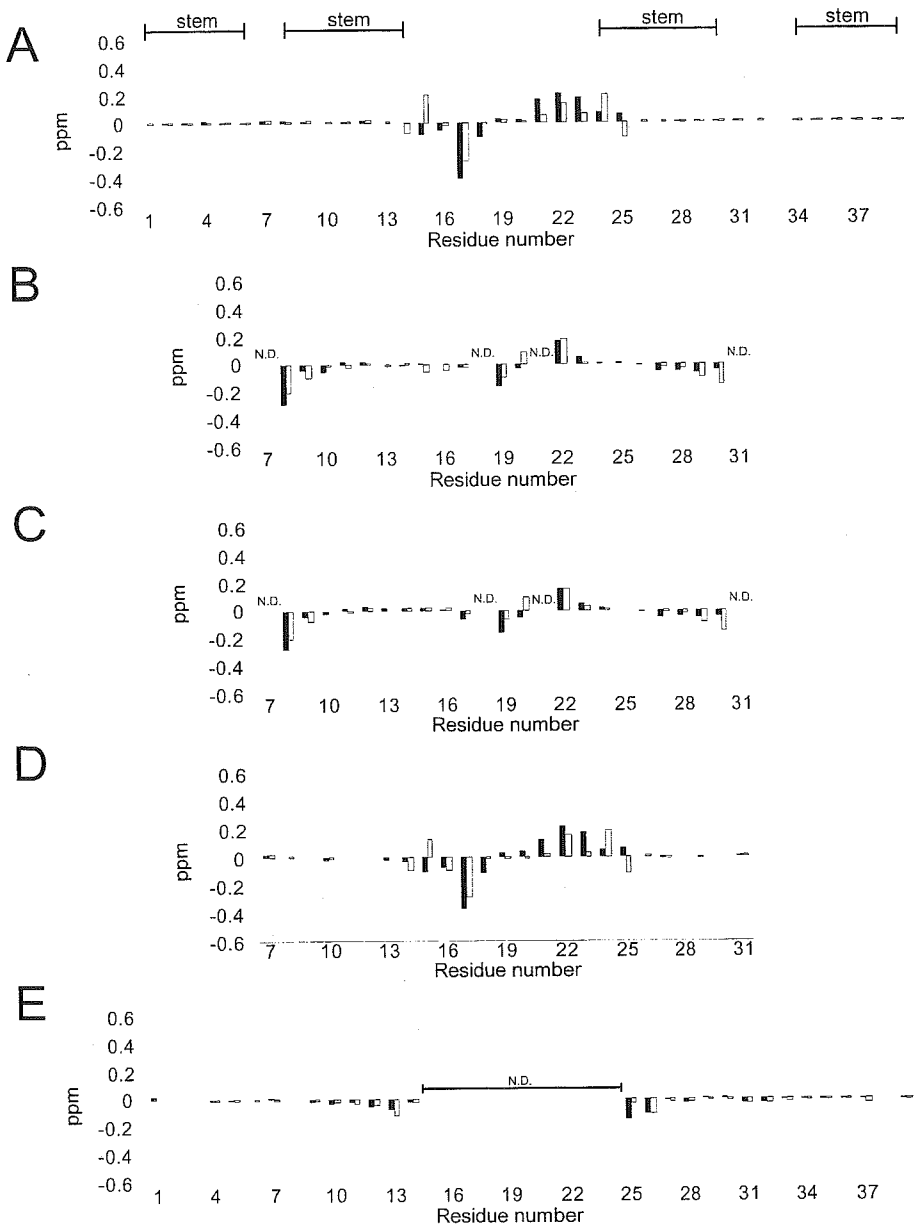


Fig. 3. **Chemical shift differences for H6/H8 and H1′.** Filled and open bars indicate H6/H8 and H1′, respectively. (A) Chemical shift differences between the kissing-loop and extended-duplex dimers of DIS39. Lines above the graph indicate the stem regions. (B) Chemical shift differences between DIS39 and loop25 in the kissing-loop dimer (data for replaced residues 7, 18, 21 and 31 are not shown). (C) Chemical shift differences between DIS39 and loop25 in the extended-duplex dimer (data for replaced residues 7, 18, 21 and 31 are not shown). (D) Chemical shift differences between the kissing-loop and extended-duplex dimers of loop25. (E) Chemical shift differences between DIS39 and bulge34 in the kissing-loop dimer (data for residues 15–24 are not shown).

*Structure Determination—The loop region of loop25 in the kissing-loop dimer*: To determine the structure of the loop region of DIS39 in both the kissing-loop and extended-duplex dimers, the NMR signals of loop25 were further analyzed and structural information was collected. The structure of the loop region consisting of the nine nucleotide loop and the stem with four base pairs was determined as shown by the broken box in Fig. 1B. A total of 286 distance restraints, 76 hydrogen bonding distance restraints, 140 dihedral restraints (Table 1), and 136 chiral restraints were used for the structural calculation. Three NOEs in the loop region, H2(A21)–H1′(U18), H2(A21)–H1′(G19) and H2(A21)–H8(G19), were judged to be intermolecular by analysis of the imino proton spectra. Four NOEs in the stem-loop linking region were considered to be intermolecular or intramolecular based on the results of the isotope filter NMR measurement (data not shown), and it was concluded that two NOEs, H2(A23)–H1′ (G17), H2(A16)–H1′ (G16), are intermolecular and three NOE, H8(A16)–H1′ (A16), H8(A16)–H2′ (A16), are intramolecular. One NOE in the stem-loop linking region was considered to be intermolecular or intramolecular in the structure calculation, and it was concluded that this NOE, H2(A23)–H2(A15), is intramolecular. Each restraint is used twice for two molecules. The structures were calculated by the restrained molecular dynamic calculation with the simulated annealing method. The structure was defined with a heavy atom r.m.s.d. of 2.14 Å for the ten converged structures (Fig. 4A, left panel), and the minimized average structure is shown in Fig. 4A (right panel). Although the overall convergence was not very good, the self-complementary region was well defined with 0.76 Å, and the stem-loop linking region was defined with 1.86 Å. The structural statistics are summarized in Table 1.

*The loop region of loop25 in the extended-duplex dimer*: The loop region of loop25 in the extended-duplex dimer was

Table 1. **NMR restraints and structural statistics.**

| | Number of restraints | | |
|---|---|---|---|
| | loop25 in the kissing-loop dimer (17 mer × 2) | loop25 in the extended-duplex dimer (17 mer × 2) | bulge34 (30 mer) |
| Distance restraints | 286 | 384 | 345 |
| imino-imino | 12 | 12 | 10 |
| intra residue | 154 | 182 | 163 |
| intra molecule | 106 | 174 | 170 |
| inter molecule | 12 | 16 | – |
| >5 Å | 2 | 0 | 2 |
| Hydrogen bonding distance restraints | 76 | 76 | 58 |
| Dihedral restraints | 140 | 138 | 126 |
| 3′-*endo* | 30 | 30 | 28 |
| 2′-*endo* | 2 | 0 | 0 |
| RNA-A stems | 108 | 108 | 98 |
| r.m.s.d. from the idealized geometry (Å) | | | |
| Bonds (Å) | 0.00897 ± 0.00004 | 0.00803 ± 0.00020 | 0.00775 ± 0.00015 |
| Angle (°) | 2.43 ± 0.23 | 2.33 ± 0.05 | 2.24 ± 0.07 |
| Impropers (°) | 1.57 ± 0.10 | 1.82 ± 0.64 | 1.53 ± 0.21 |
| Heavy-atoms r.m.s.d. (Å)[a] | | | |
| All | 2.14 | 1.45 | 1.98 |
| Stem-loop linking region[b] | 1.86 | 1.31 | |
| Bulge region[c] | | | 1.90 |

[a]Averaged r.m.s.d. between an average structure and the 10 converged structures were calculated. The converged structures did not contain experimental distance violations >0.2 Å or dihedral violations >5°, [b]The stem-loop linking region consists of residues 14 to 17, 22 to 24, 14* to 17* and 22* to 24*, [c]The bulge region consists of residues 6 to 10 and 28 to 34. Asterisks indicate residues in the other molecule.

determined (broken box in Fig. 1B). A total of 384 distance restraints, 76 hydrogen bonding distance restraints, 138 dihedral restraints (Table 1) and 136 chiral restraints were used for the structure calculation. For the stem-loop linking region, H2 of A23 was connected by intermolecular NOEs to H1′ and H2 of A15, H2 of A16 and H1′ of G17. The structures were calculated by the restrained molecular dynamic calculation with the simulated annealing method described above. The structure was well defined with a heavy atom r.m.s.d. of 1.45 for the ten converged structures (Fig. 4B, left panel), and the minimized average structure is shown in Fig. 4B (right panel). The stem-loop linking region was defined with 1.31 Å. The structural statistics are summarized in Table 1.

*The stem-bulge-stem region of bulge34*: A structural determination was performed for bulge34 except for the UUCG loop (broken box in Fig. 1C). A total of 345 distance restraints, 58 hydrogen bonding distance restraints, 126 dihedral restraints (Table 1) and 120 chiral restraints were used for the structure calculation. Two NOE restraints (>5 Å), H2(A31)–H1′(U9) and H1′(A31)–H1′(U9), were added to the distance restraints based on the absence of NOE cross peaks. The structures were calculated by the restrained molecular dynamic calculation with a simulated annealing protocol. The structure was defined with a heavy atom r.m.s.d. of 1.98 for the ten converged structures (Fig. 4C, left panel), and the minimized average structure is shown in Fig. 4C (right panel). Although the overall convergence is not very good, the stem regions are well defined with 0.83 or 0.78 Å, respectively. The bulge region was defined with 1.90 Å. The structural statistics are summarized in Table 1.

*The two types of dimers of DIS39*: Solution structures of DIS39 were then constructed by combining the structure parts. The structures of the kissing-loop or extended-duplex dimer region and stem-bulge-stem region were combined by superimposing two base pairs, C12:G26 and U13:G25 (Fig. 1, gray area). The left panels of Fig. 5 show the ten structures prepared by using the minimized average structure of the stem-bulge-stem region (Fig. 4C, right) and each of the ten lowest energy structures of the loop region (Fig. 4, A or B, left) superimposed by the loop region. The right panels of Fig. 5 show the structures prepared using the minimized average structure of the stem-bulge-stem region (Fig. 4C, right) and the loop region (Fig. 4, A or B, right). The relative angles between the stem-bulge-stem regions differ between the kissing-loop and extended-duplex dimers as shown in the right panels of Fig. 5. However, the fluctuations of the relative angles are rather large and the ranges overlap between the two dimers as shown in the left panels of Fig. 5. In fact, the values of the residual dipolar coupling for the stem-bulge-stem region are similar between the kissing-loop and extended-duplex dimers (to be published). A preliminary normal mode analysis suggested the existence of hinge motion, and, in order to reveal the dynamic properties of the dimers, a molecular dynamics analysis, as well as the thermodynamics analysis (*33*), is required. The most obvious local difference was observed for A16; for the kissing-loop dimer, A16 was close to the same residue in the other molecule (Fig. 6A, left) and did not stack above A15 of the same molecule nor G17 of the other molecule (Fig. 6A, right), whereas for the extended-duplex dimer, A16 was apart from the same residue of the other molecule (Fig. 6B, left) and stacked between A15 and G17 (Fig. 6B, right).

*Structural Comparison with Related Structures*—Ennifar *et al.* (*20*) determined the crystal structure of

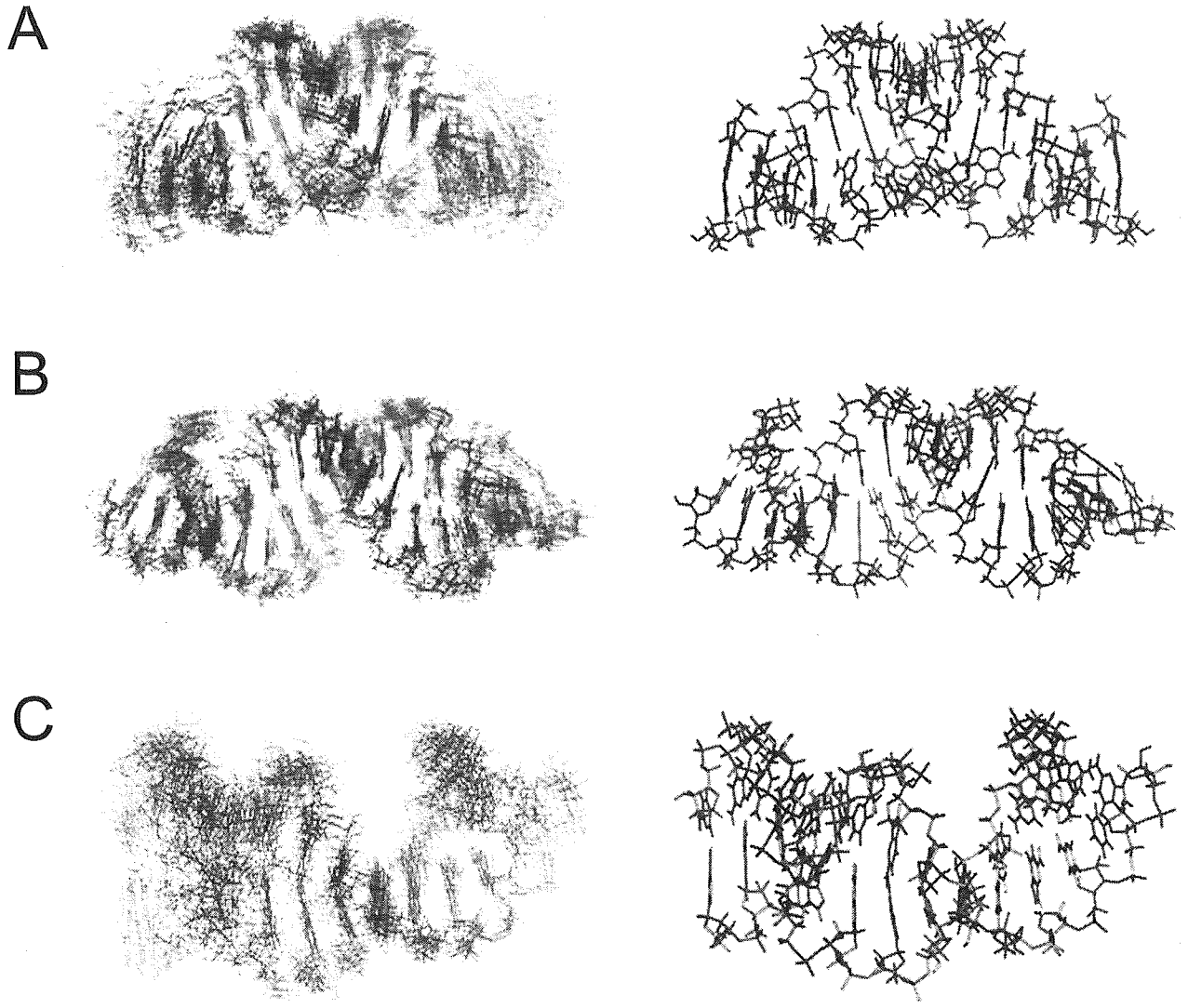


Fig. 4. **Solution structures of each part of DIS39.** Left panels show the superimposition of the 10 lowest energy structures and the right panels show the minimized average structures. (A) The loop region of loop25, as shown by the broken box in Fig. 1b, in the kissing-loop dimer. Each strand is colored in red or blue. (B) The loop region of loop25 in the extended-duplex dimer. (C) The stem-bulge-stem region of bulge34.

the kissing-loop dimer. The present structure is similar to the crystal structures in general, except for A15 and A16. In the present structure, A15 stacks on G14 and A16 interacts with the same residue in the other molecule (Fig. 6A, right). On the other hand, in the crystal structure, A15 and G16 are flipped out (*20*). It is noted that the numbering system of DIS39 is used for other structures for convenience, and position 16 is occupied by A or G depending on the strain. A15 and A16 (or G16) might be flexible and can be flipped out even in solution. Mujeeb *et al.* (*19*) determined the solution structure of the kissing-loop dimer. In this structure, A16 interacts with A15 and C24 in the other molecule, and, as a result, the distance between the two stems is relatively short. Thus, this restricted interaction makes the global structure different from the present structure and the crystal structure. However, the location of A15 is similar in the two solution structures. The difference in the conformation of A16 between the two solution structures may reflect the difference in the sequence of the stem adjacent to the loop and/or in the sample condition, including the salt concentration. The NOE connectivity determined in the present study agrees in general with those of Dardel *et al.* who analyzed the structure of the stem-loop region in the kissing-loop dimer by NMR (*34*).

Girard *et al.* (*21*) and Mujeeb *et al.* (*22*) determined the solution structures of extended-duplex dimers. In these two structures, as well as in the present structure, A15, A16 and A23 form a zipper like structure (Fig. 6B, right). On the other hand, in the case of the crystal structure of the extended-duplex dimer, G16 forms a G:A base pair and A15 is flipped out, and it was assumed that this in-out bulge transconformation is magnesium-dependent (*23*).

Structures of the stem-bulge-stem region were shown by Lawrence *et al.* (*26*) and Yuan *et al.* (*27*). In the solution structure determined by Lawrence *et al.* (*26*), continuous stackings were formed for each strand, G6-C8 and

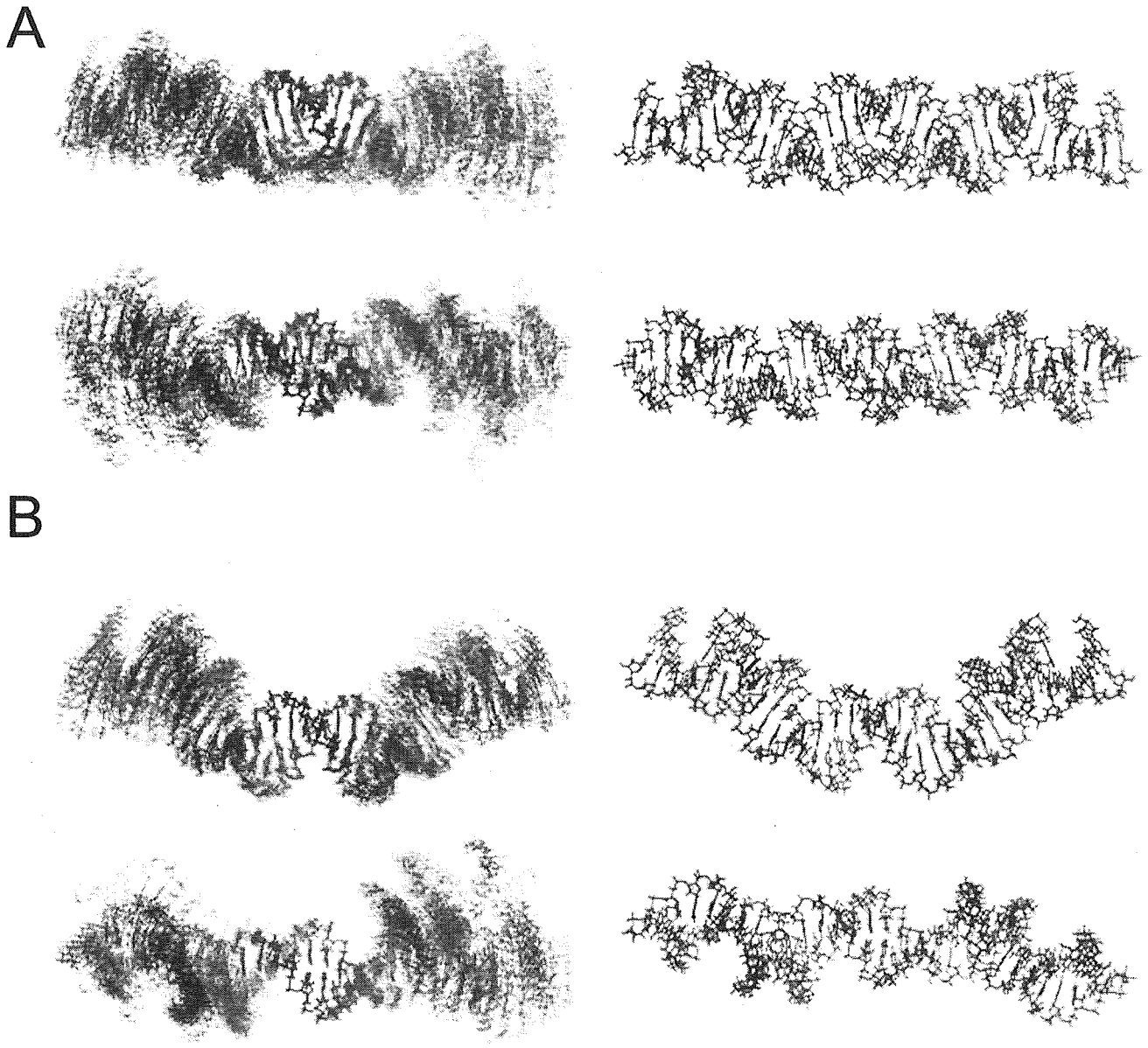


Fig. 5. **Solution structures of the (A) kissing-loop and (B) extended-duplex dimers of DIS39.** Left panels show the structures constructed by combining the structures of the loop (the 10 lowest energy structures of the kissing-loop or extended-duplex dimers) and the stem-bulge-stem (minimized average structure) regions. Right panels show the structures constructed by combining the minimized average structures of the loop and stem-bulge-stem regions. The two regions were combined by superimposing two base pairs, C12–G26 and U13–G25 (Fig. 1, gray area). Each strand is colored in red or blue and views from two different directions are shown.

G30-C34. Yuan *et al.* (*27*) showed that G7 and A31 form a base pair, and that G33 is not always stacked on G32 or C34, and, in general, the present structure is identical to the latter structure. Greatorex *et al.* (*25*) showed that the bulge region is too flexible to determine the conformation. These conformational differences may be caused by differences in the stability of the terminal stem. Lawrence *et al.* (*26*) adopted a stable 7 base-pair stem, and their structure forms an ordered conformation in the bulge region. In contrast, Greatorex *et al.* (*25*) adopted an unstable 4 base-pair stem and the bulge region is flexible. Yuan *et al.* (*27*) adopted a 4 base-pair stem and a flanking adenosine residue at the 3′ terminal that must stabilize the stem. In the present study, a 6 base-pair stem was used.

*Mechanism of the Two Stem Dimerization*—Between the kissing-loop and extended-duplex dimers, A16 shows the most drastic change in interaction with other residues, suggesting that A16 is the key residue in the two step dimerization reaction. The difference in the A16 conformation among structures with different sequences and determined under different conditions as described above, also suggests the importance of this residue. Mujeeb *et al.* (*19*, *22*) also pointed out the flexibility around the junction of the loop and the stem of DIS in the kissing-loop and

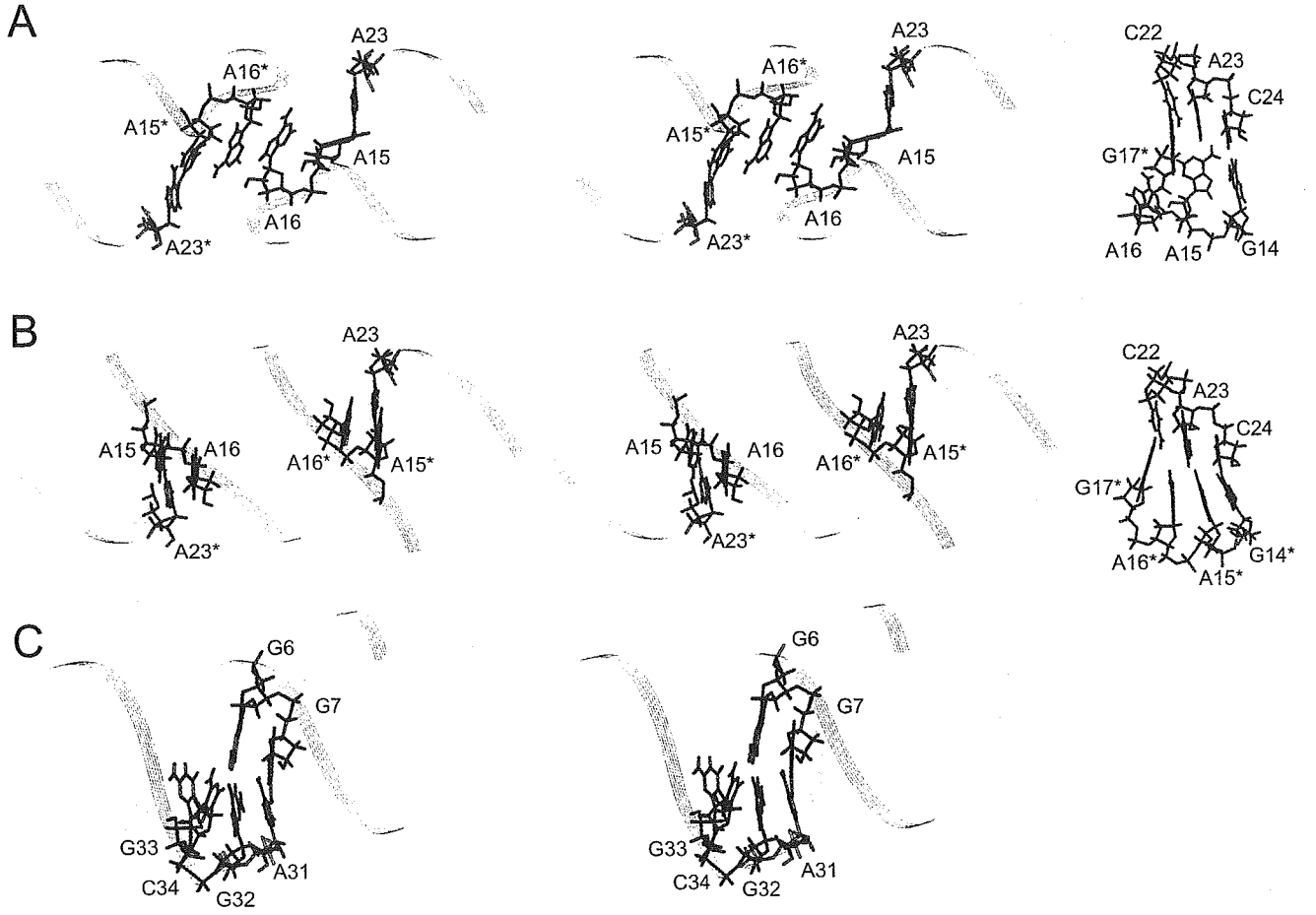


Fig. 6. **Structures of the linking regions.** (A) Regions linking the stem and loop in the kissing-loop dimer. The left panels show the positions of A15, A16, and A23 in the entire structure in a stereo view, and the right panels show residues linking the stem and loop. Asterisks indicate residues in the other strand. (B) Regions linking the stem and loop in the extended-duplex dimer. (C) The bulge region linking the two stems.

extended-duplex dimers. Imino proton signals due to U9:A29 and U10:A28 are much broader than other signals in the stem region, and no imino proton signal due to C8:G30 was observed. Thus, the stem between the loop and bulge is destabilized by the bulge region. Our previous experiments also showed that the bulge region is required for the two-step dimerization to adjust the thermal stability of DIS, and Greatorex *et al.* (*25*) also indicated that the flexibility of the bulge region is critical based on the fact that mutations in the bulge region strongly affect the melting temperature, as well as the fact that none of the wild-type sequences in the bulge region that increase the melting temperature is ever found in wild-type viruses. Thus, the conformational conversion from the kissing-loop dimer to the extended-duplex dimer might require two factors, the movement of A16 and the modest stability of the stem caused by the presence of the bulge region.

In the present study, a set of structures corresponding to the initial and final structures of the two-step dimerization of DIS are provided; these structures will promote studies to elucidate the molecular mechanism of the conformational change in the two-step dimerization, including an analysis of the interaction between DIS and NCp7, in addition to the molecular dynamics approach.

*Coordinates*: The structure has been deposited in the Protein Data Bank (accession code 2D17: the stem-bulge-stem region of bulge34, 2D18: the extended-duplex dimer of loop25, 2D19: the kissing-loop dimer of loop25, 2D1A: the extended-duplex dimer of DIS39 and 2D1B: the kissing-loop dimer of DIS39).

This work was supported by the "Research for the Future" Program (JSPS-RFTF97L00503) from the Japan Society for the Promotion of Science, and, in part, by a Grant-in-Aid for High Technology Research from the Ministry of Education, Science, Sports and Culture, Japan.

REFERENCES

1. Hoglund, S., Ohagen, A., Goncalves, J., Panganiban, A.T., and Gabuzda, D. (1997) Ultrastructure of HIV-1 genomic RNA. *Virology* **233**, 271–279
2. Laughrea, M., Jette, L., Mak, J., Kleiman, L., Liang, C., and Wainberg, M.A. (1997) Mutations in the kissing-loop hairpin of human immunodeficiency virus type 1 reduce viral infectivity as well as genomic RNA packaging and dimerization. *J. Virol.* **71**, 3397–3406
3. Clever, J.L. and Parslow, T.G. (1997) Mutant human immunodeficiency virus type 1 genomes with defects

in RNA dimerization or encapsidation. *J. Virol.* **71**, 3407–3414
4. Paillart, J.C., Berthoux, L., Ottmann, M., Darlix, J.L., Marquet, R., Ehresmann, B., and Ehresmann, C. (1996) A dual role of the putative RNA dimerization initiation site of human immunodeficiency virus type 1 in genomic RNA packaging and proviral DNA synthesis. *J. Virol.* **70**, 8348–8354
5. Laughrea, M. and Jette, L. (1994) A 19-nucleotide sequence upstream of the 5′ major splice donor is part of the dimerization domain of human immunodeficiency virus 1 genomic RNA. *Biochemistry* **33**, 13464–13474
6. Skripkin, E., Paillart, J.C., Marquet, R., Ehresmann, B., and Ehresmann, C. (1994) Identification of the primary site of the human immunodeficiency virus type 1 RNA dimerization *in vitro*. *Proc. Natl. Acad. Sci. USA* **91**, 4945–4949
7. Fu, W. and Rein, A. (1993) Maturation of dimeric viral RNA of Moloney murine leukemia virus. *J. Virol.* **67**, 5443–5449
8. Fu, W., Gorelick, R.J., and Rein, A. (1994) Characterization of human immunodeficiency virus type 1 dimeric RNA from wild-type and protease-defective virions. *J. Virol.* **68**, 5013–5018
9. Laughrea, M. and Jette, L. (1996) Kissing-loop model of HIV-1 genome dimerization: HIV-1 RNAs can assume alternative dimeric forms, and all sequences upstream or downstream of hairpin 248–271 are dispensable for dimer formation. *Biochemistry* **35**, 1589–1598
10. Muriaux, D., Fosse, P., and Paoletti, J. (1996) A kissing complex together with a stable dimer is involved in the HIV- 1Lai RNA dimerization process *in vitro*. *Biochemistry* **35**, 5075–5082
11. Muriaux, D., Girard, P.M., Bonnet-Mathoniere, B., and Paoletti, J. (1995) Dimerization of HIV-1Lai RNA at low ionic strength. An autocomplementary sequence in the 5′ leader region is evidenced by an antisense oligonucleotide. *J. Biol. Chem.* **270**, 8209–8216
12. Laughrea, M., Shen, N., Jette, L., Darlix, J., Kleiman, L., and Wainberg, M.A. (2001) Role of distal zinc finger of nucleocapsid protein in genomic RNA dimerization of human immunodeficiency virus type 1; No role for the palindrome crowning the R-U5 hairpin. *Virology* **281**, 109–116
13. de Guzman, R.N., Wu, Z.R., Stalling, C.C., Pappalardo, L., Borer, P.N., and Summers, M.F. (1998) Structure of the HIV-1 nucleocapsid protein bound to the SL3 ψ–RNA recognition element. *Science* **279**, 384–388
14. Amarasinghe, G.K., de Guzman, R.N., Turner, B.G., Chancellor, K.J., Wu, Z.R., and Summers, M.F. (2000) NMR structure of the HIV-1 nucleocapsid protein bound to Stem-Loop SL2 of the ψ–RNA packaging signal. Implications for Genome recognition. *J. Mol. Biol.* **301**, 491–511
15. Berkowitz, R., Fisher, J., and Goff, S.P. (1996) RNA packaging. *Curr. Top. Microbiol. Immunol.* **214**, 177–218
16. Darlix, J.L., Lopez-Lastra, M., Mély, Y., and Roques, B. (2003) Nucleocapsid protein chaperoning of nucleic acids at the heart of HIV structure, assembly and cDNA synthesis. In *HIV Sequence Compendium 2002* (Kuiken, C., Foley, B., Freed, E., Hahn, B., Marx, P., McCutchan, F., Mellors, J.W., Wolinsky, S., and Korber, B., eds.) pp. 69–88, Los Alamos National Laboratory, Los Alamos, NM
17. Takahashi, K., Baba, S., Koyanagi, Y., Yamamoto, N., Takaku, H., and Kawai, G. (2001) Two basic regions of NCp7 are sufficient for conformational conversion of HIV-1 dimerization initiation site from kissing-loop dimer to extended-duplex dimer. *J. Biol. Chem.* **276**, 31274–31278
18. Baba, S., Takahashi, K., Koyanagi, Y., Yamamoto, N., Takaku, H., Gorelick, R.J., and Kawai, G. (2003) Role of the Zinc Fingers of HIV-1 Nucleocapsid Protein in Maturation of Genomic RNA. *J. Biochem.* **134**, 637–639
19. Mujeeb, A., Clever, J.L., Billeci, T.M., James, T.L., and Parslow, T.G. (1998) Structure of the dimer initiation complex of HIV-1 genomic RNA. *Nat. Struct. Biol.* **5**, 432–436
20. Ennifar, E., Walter, P., Ehresmann, B., Ehresmann, C., and Dumas, P. (2001) Crystal Structures of Coaxially-Stacked Kissing Complexes of the HIV-1 RNA Dimerization Initiation Site. *Nat. Struct. Biol.* **8**, 1064–1068
21. Girard, F., Barbault, F., Gouyette, C., Huynh-Dinh, T., Paoletti, J., and Lancelot, G. (1999) Dimer Initiation Sequence of HIV-1Lai Genomic RNA: NMR Solution Structure of the Extended Duplex. *J. Biomol. Struct. Dyn.* **16**, 1145–1157
22. Mujeeb, A., Parslow, T.G., Zarrinpar, A., Das, C., and James, T.L. (1999) NMR structure of the mature dimer initiation complex of HIV-1 genomic RNA. *FEBS Lett.* **458**, 387–392
23. Ennifar, E., Yusupov, M., Walter, P., Marquet, R., Ehresmann, B., Ehresmann, C., and Dumas, P. (1999) The crystal structure of the dimerization initiation site of genomic HIV-1 RNA reveals an extended duplex with two adenine bulges. *Structure Fold Des.* **7**, 1439–1449
24. Ennifar, E., Walter, P., and Dumas, P. (2003) A Crystallographic Study of the Binding of 13 Metal Ions to Two Related RNA Duplexes. *Nucleic Acids Res.* **31**, 2671–2682
25. Greatorex, J., Gallego, J., Varani, G., and Lever, A. (2002) Structure and Stability of Wild-Type and Mutant RNA Internal Loops from the SL-1 Domain of the HIV-1 Packaging Signal. *J.Mol.Biol.* **322**, 543–557
26. Lawrence, D.C., Stover, C.C., Noznitsky, J., Wu, Z., and Summers, M. F. (2003) Structure of the Intact Stem and Bulge of HIV-1 Psi-RNA Stem-Loop Sl1. *J. Mol. Biol.* **326**, 529–542
27. Yuan, Y., Kerwood, D.J., Paoletti, A.C., Shubsda, M.F., and Borer, P.N. (2003) Stem of SL1 RNA in HIV-1: structure and nucleocapsid protein binding for a 1 × 3 internal loop. *Biochemistry* **42**, 5259–5269
28. Shen, N., Jette, L., Liang, C., Wainberg, M.A., and Laughrea, M. (2000) Impact of human immunodeficiency virus type 1 RNA dimerization on viral infectivity and of stem-loop B on RNA dimerization and reverse transcription and dissociation of dimerization from packaging. *J. Virol.* **74**, 5729–5735
29. Takahashi, K.I., Baba, S., Chattopadhyay, P., Koyanagi, Y., Yamamoto, N., Takaku, H., and Kawai, G. (2000) Structural requirement for the two-step dimerization of human immunodeficiency virus type 1 genome. *RNA* **6**, 96–102
30. Varani, G., Aboul-era, F., and Allain, F.H.-T. (1996) NMR investigation of RNA structure. *Prog. NMR Spect.* **29**, 51–127
31. Takahashi, K., Baba, S., Hayashi, S., Koyanagi, Y., Yamamoto, N., Takaku, H., and Kawai, G. (2000) NMR analysis on intra- and inter-molecular stems in the dimerization initiation site of the HIV-1 genome. *J. Biochem.* **127**, 681–639
32. St.Louis, D.C., Gotte, D., Sanders-Buell, E., Ritchey, D.W., Salminen, M.O., Carr, J.K., and McCutchan, F.E. (1998) Infectious molecular clones with the nonhomologous dimer initiation sequences found in different subtypes of human immunodeficiency virus type 1 can recombine and initiate a spreading infection in vitro. *J. Virol.* **72**, 3991–3998
33. Weixlbaumer, A., Werner, A., Flamm, C., Westhof, E., and Schroeder, R. (2004) Determination of thermodynamic parameters for HIV DIS type loop-loop kissing complexes. *Nucleic Acids Res.* **32**, 5126–5133
34. Dardel, R., Marguet, R., Ehresmann, C., Ehresmann, B., and Blanquet, S. (1998) Solution studies of the dimerization initiation site of HIV-1 genomic RNA. *Nucleic Acids Res.* **26**, 3567–3571

# Ku80 autoantigen as a cellular coreceptor for human parvovirus B19 infection

Yasuhiko Munakata, Takako Saito-Ito, Keiko Kumura-Ishii, Jie Huang, Takao Kodera, Tomonori Ishii, Yasuhiko Hirabayashi, Yoshio Koyanagi, and Takeshi Sasaki

**Human parvovirus B19 (B19) infects human erythroid cells expressing P antigen. However, some cell lines that were positive for P antigen failed to bind B19, whereas some cell lines had an ability to bind B19 despite undetectable expression of P antigen. We here demonstrate that B19 specifically binds with Ku80 autoantigen on the cell surface. Furthermore, transfection of HeLa cells with the gene of Ku80 enabled the binding of B19 and allowed its entry into cells. Moreover, reduction of cell-surface expression of Ku80 in KU812Ep6 cells, which was a high-sensitive cell line for B19 infection, by short interfering RNA for Ku80 resulted in the marked inhibition of B19 binding in KU812Ep6 cells. Although Ku80 originally has been described as a nuclear protein, human bone marrow erythroid cells with glycophorin A or CD36, B cells with CD20, or T cells with CD3 were all positive for cell-surface expression of Ku80. B19 infection of KU812Ep6 cells and bone marrow cells was inhibited in the presence of anti-Ku80 antibody. Our data suggest that Ku80 functions as a novel coreceptor for B19 infection, and this finding may provide an explanation for the pathologic immunity associated with B19 infection. (Blood. 2005;106: 3449-3456)**



## Introduction

Human parvovirus B19 (B19) infects erythroid-lineage cells through P antigen and causes various clinical symptoms such as erythema infectiosum, anemia, polyarthritis, or fetal hydrops in humans.[1,2] The cellular receptor for B19 infection has been regarded as blood group P antigen based on the failure of B19 infection in a patient with an hereditary defect of P antigen.[3] However, the target cells of B19 may be not be exclusively P-antigen–positive erythroid-lineage cells, as illustrated by the poor relationship between P antigen expression levels and the efficiency of B19 infection[4] or the failure of B19 binding to globoside.[5] Recently, Weigel-Kelley et al described the role of $\alpha5\beta1$ integrin as the cellular coreceptor for B19 infection.[6] The notion that B19 receptor is not solely P antigen may be compatible with clinical findings that B19 has been detected in mononuclear cells of blood or tonsils with acute or prolonged B19 infection.[7,8] Also, following B19 infection, the numbers of peripheral blood lymphocytes may decrease despite undetectable levels of P antigen on their cell surface.[9,10] Finally, autoimmune-like phenomena including antinuclear antibodies, rheumatoid factors, or antiphospholipid antibodies are often associated with B19 infection,[8,11] and the levels of tumor necrosis factor $\alpha$ (TNF-$\alpha$) and interferon $\gamma$ (IFN-$\gamma$) secreted from macrophages or T cells are elevated during acute or prolonged B19 infection.[12] Clinical studies have shown that B19 DNA can be amplified from joint samples by polymerase chain reaction (PCR),[13,14] and infective B19 was detected in the articular lesions of patients with rheumatoid arthritis. B19 transcripts and B19 protein viral protein 1 (VP1) were also present in T cells, B cells, macrophages, and follicular dendritic cells.[14] The cellular mechanism that may allow B19 binding and its entry into nonerythroid cells has not been elucidated. In the present study, we explored a putative receptor for B19 that was distinct from P antigen.

## Materials and methods

### Cells

Macrophage cell lines U937, urinary bladder carcinoma cell line T24, colon cancer cell line SW620, renal adenocarcinoma cell line ACHN, and HeLa cells were provided by the Cell Resource Center for Biomedical Research, Institute of Development, Aging and Cancer, Tohoku University (Sendai, Japan). Human erythroid cell line KU812Ep6[15] was provided by E. Miyagawa (Institute of Fuji Rebio, Tokyo, Japan). T-cell line H9 was purchased from American Type Culture Collection (Manassas, VA). Bone marrow samples were obtained from the volunteers who gave informed consent for the use of their samples for our study. Informed consent was provided in accordance with the Declaration of Helsinki.

### Human parvovirus B19

Serum from patient 1 with acute B19 infection was used as the source for B19 in the in vitro infection study. The serum contained $2.5 \times 10^{14}$ copies of B19-DNA per milliliter but was negative for IgM and IgG anti-B19 antibodies.[16] B19 was purified using cellulose hollow fiber, was provided by Dr. K. Yamaguchi,[17] and used as an antigen for enzyme-linked immunosorbent assay (ELISA).

From the Department of Rheumatology and Hematology, and Department of Virology, Tohoku University Graduate School of Medicine, Sendai, Japan.

Submitted February 8, 2005; accepted July 5, 2005. Prepublished online as *Blood* First Edition Paper, August 2, 2005; DOI 10.1182/blood-2005-02-0536.

Supported by a Grant-in-Aid for Scientific Research (A) from the Ministry of Education, Science, Sports and Culture in Japan.

Y.M. and T.S.-I. designed with research, performed research, and wrote the paper; K.K.-I., J.H., T.K., and T.I. performed research; Y.H. analyzed data; and Y.K. and T.S. designed research.

Y.M. and T.S.-I. contributed equally to this work.

**Reprints:** Yasuhiko Munakata, Department of Rheumatology and Hematology, Tohoku University Graduate School of Medicine, 1-1 Seiryo-cho, Aoba-ku, Sendai 980-8574, Japan; e-mail: mnkt@mail.tains.tohoku.ac.jp.

The publication costs of this article were defrayed in part by page charge payment. Therefore, and solely to indicate this fact, this article is hereby marked "advertisement" in accordance with 18 U.S.C. section 1734.

### Recombinant human parvovirus B19 empty capsid protein

Recombinant human parvovirus B19 empty capsid protein (rB19ECP), prepared as described previously,[18] was kindly provided by K. Kamata at Denka Seiken (Tokyo, Japan). rB19ECP was composed of VP1 and VP2 at a ratio of 5:95, respectively.

### Antibodies

Monoclonal anti-Ku80 antibodies that recognized N-terminus (amino acids 3-22) or C-terminus of Ku80 (amino acids 610-705) were purchased from Oncogene (Boston, MA) and BD Biosciences (San Jose, CA), respectively. PAR3 is a mouse monoclonal antibody recognizing VP2, which shared with VP1 of B19.[19,20] 1F5 is a mouse monoclonal antibody with anti-idiotypic activity to an anti-DNA antibody,[21] which was used as a control for flow cytometry analysis. GL4, a rabbit polyclonal antigloboside antibody (IgG and IgM), was purchased from Matreya (State College, PA). Monoclonal anti–α5 and anti–β1 integrin antibodies were purchased from Chemicon (Temecula. CA). Other monoclonal antibodies were purchased from BD Biosciences.

### In vitro infection of B19

Cells ($2 \times 10^6$) in 0.5 mL RPMI were infected with B19 containing serum from 1 (diluted at $2 \times 10^{11}$ copies of B19 DNA/mL) for 30 minutes on ice and washed extensively 3 times with phosphate-buffered saline (PBS), pH 7.2, for evaluation of B19 adsorption. To study B19 replication, the prepared cells in 3 mL RPMI containing 10% fetal bovine serum (FBS) were further incubated at 37°C for 48 hours in a 5% $CO_2$ humidified atmosphere, followed by 3 extensive washes with PBS and then evaluated for B19 protein and B19 DNA.

### Protein precipitation and purification of precipitated protein

Cell-surface protein of H9 cells was labeled with sulfo-NHS esters of biotin (Pierce, Rockford, IL), followed by protein precipitation. H9 cells were treated with Nonidet P-40 lysis buffer (1% Nonidet P-40, 140 mM NaCl, 1 mM phenylmethylsulfonyl fluoride [PMSF], 5 mM EDTA [ethylenediaminetetraacetic acid], 50 mM Tris [tris(hydroxymethyl)aminomethane)–HCl, pH 7.4) and immunoprecipitated with rB19ECP- or bovine serum albumin (BSA)–conjugated cyanogen bromide (CNBr)–Sepharose (Amersham Bioscience, Piscataway, NJ). The precipitated samples were separated under denaturing conditions in a 7.5% sodium dodecyl sulfate–polyacrylamide gel electrophoresis (SDS-PAGE) gel, followed by electrotransfer to a polyvinylidene difluoride (PVDF) membrane. Protein was detected with enhanced chemiluminescence (ECL) Western blotting detection system (Amersham Biosciences) and visualized by LAS-1000 (Fujifilm, Tokyo, Japan). A crude membrane fraction of H9 cells ($1 \times 10^{11}$) was prepared and solubilized in 1% Nonidet P-40 lysis buffer. The fraction was then precipitated with rB19ECP-conjugated CNBr-Sepharose for 16 hours at 4°C, and the precipitated proteins were separated by SDS-PAGE followed by Coomassie blue staining. Protein sequencing was carried out by Toray Research Center (Kamakura, Japan).

### Flow cytometry analysis

Cells were suspended in 100 μL 1% BSA-PBS and incubated with 5 μg/mL test antibodies on ice for 30 minutes. Cells were then washed 3 times with PBS. Cells that required secondary antibodies for detection were further incubated with fluorescein isothiocyanate (FITC)–conjugated goat anti–mouse IgG (or FITC-conjugated anti–rabbit IgG for the GL4 primary antibody; Sigma, St Louis, MO) at 1:200 on ice for 30 minutes. Cells were washed 3 times with PBS before flow cytometry analysis (Becton Dickinson, San Jose, CA). For the detection of Ku80 on the cell surface of bone marrow cells, cells were first reacted with 5 μg/mL anti-Ku80 antibody followed by an incubation with FITC-conjugated anti–mouse IgG antibody. After being washed, cells were reacted with the cell-lineage–specific antibodies (anti–glycophorin A, anti-CD3, anti-CD20, anti-CD56, anti-CD14, or anti-CD36 antibodies) conjugated with phycoerythrin (PE; BD Biosciences) according to the manufacturer's instruction.

In the in vitro infection study, B19-infected cells were fixed with 4% paraformaldehyde followed by permeabilization with SAP buffer (0.1% saponin, 0.05% $NaN_3$ in Hanks balanced salt solution). Next, cells were incubated with PAR3 at a concentration of 5 mg/mL on ice for 30 minutes, followed by the same procedure as described.

### ELISA and quantitative PCR

ELISA was carried out by using rB19ECP-fixed microwells (Denka Seiken). The basic protocol for ELISA and quantitative PCR for measuring B19-DNA was performed as described before.[15,16]

### Preparation of cell fraction from B19-infected cells

Cells ($6 \times 10^5$) were infected with B19 for 30 minutes on ice. Following three washes with PBS, pH 7.2, DNA was extracted from $2 \times 10^5$ cells to measure adsorbed B19. The remaining $4 \times 10^5$ cells were further incubated for 30 minutes at 37°C, followed by 3 washes with PBS, pH 4.5. To obtain cytoplasm fractions of B19-infected cells, cells were treated with lysis buffer A (100 mM Tris-HCl, pH 7.5, 1% Triton X-100, 5 mM EDTA, 50 mM NaCl, and 100 μM PMSF), and centrifuged. Then, DNA was extracted from the supernatant to measure B19-DNA in cytoplasm. The pellets were washed with lysis buffer A 3 times and treated with lysis buffer B (100 mM Tris-HCl, pH 7.5, 1% Triton X-100, 5 mM EDTA, 500 mM NaCl, and 100 μM PMSF). Following centrifugation, DNA was extracted from the supernatant to measure B19-DNA in nuclei.

### Transfection

Five micrograms of expression vector pcD[22] containing pKu80 was used for the transfection of $1 \times 10^5$ HeLa cells, and pcD was used as a vector-only control. Transfection was done using the lipofectin method (Invitrogen, Carlsbad, CA). Transfected HeLa cells were infected with B19 for 30 minutes at 37°C. After being washed 3 times with PBS, pH 7.2, cells were collected with 5 mM EDTA-PBS, and B19 was detected by confocal microscopy analysis. Transfected HeLa cells were incubated with 1 μg/mL biotinylated rB19ECP in the presence of 5 μg/mL inhibitor antibodies for 30 minutes at 37°C. After being washed 3 times with PBS, pH 7.2, cells were collected with 5 mM EDTA-PBS, and rB19ECP or Ku80 was detected by confocal microscopy analysis.

### RNA interference of K80 in KU812Ep6

The short interfering RNA (siRNA) for Ku80 was synthesized targeting the sequence between nucleotide numbers 130 and 148: 5′-CAAGCAAA-GAAGGUGAUAAdTdT-3′ (sense), 3′-dTdTGUUCGUUUCUUCCAC-UAUU-5′ (antisense). Disordered siRNA of scrambled nucleotide sequence, used as negative control, was 5′-GCGCGCUUUGUAGGAUUCG-dTdT-3′ (sense), 3′-dTdTCGCGCGAAACAUCCUAAGC-5′ (antisense). Synthesized siRNA (200 nM) was transfected to $1 \times 10^6$ KU812Ep6 cells by Cell Line Nucleofector Kit V (Amaxa, Gaithersburg, MD) according to the manufacturer's instructions. Transfected cells were subjected to flow cytometry analysis and in vitro infection study of B19, after 48 hours of incubation.

### Detection of B19 in HeLa cells by confocal laser microscopy

Cells were grown on glass microslides and fixed with 4% paraformaldehyde in PBS for 10 minutes at room temperature. Cells were blocked with PBS containing 10% FBS for 30 minutes at 4°C, followed by incubation with mouse monoclonal anti-B19 antibody PAR3 (10 μg/mL) for 30 minutes at 4°C, then washed with PBS twice, and incubated with FITC-conjugated goat anti–mouse IgG (1:100; Sigma) for 30 minutes at 4°C. To detect localization of Ku80 and rB19ECP, cells on glass microslides were incubated with mouse monoclonal anti-Ku80 antibody (5 μg/mL) for 30 minutes at 4°C, washed with PBS twice, and incubated with tetramethyl isothiocyanate (TRITC)–conjugated goat anti–mouse IgG (1:50; Sigma) for 30 minutes at 4°C; cells were further incubated with avidin-FITC (1:100; Gibco, Carlsbad, CA) for 30 minutes at 4°C for the detection of labeled

rB19ECP. Confocal miscroscopy analysis was performed with a D-ECLIPSE CI (Nikon, Kawasaki, Japan) mounted with 20×/0.50 or 40×/0.75 Plan Fluor dry objective lenses. Excitation at 488 nm from an argon laser and at 543 nm from a helium-neon laser was used. Images were acquired with E2-CI 2.00 software (Nikon) and processed with Adobe Photoshop 7.0.1 (Adobe Systems, San Jose, CA).

## Results

### Identification of B19-binding protein on the cell surface of nonerythroid cells

To identify a putative receptor for B19, we first checked the expression of P antigen (Figure 1). Flow cytometry analysis revealed that α5β1 integrin[6] was also positive on the surface of all cell lines tested (data not shown). We then studied the binding and replication of B19 in association with the expression of P antigen and α5β1 integrin. Quantitative study for cell-surface binding, B19 DNA replication, and fluorescence-activating cell sorting (FACS) analysis using anti–B19 protein (VP2) antibody PAR3 revealed that B19 binds not only to a P antigen–expressing erythroid cell line KU812Ep6 but also to a macrophage cell line, U937, to a T-cell line, H9, and a renal carcinoma cell line, ACHN, in which P antigen was undetectable on the cell surface. None of the cell lines, T24, SW620, and HeLa, bound B19 despite surface P antigen expression (left column in Figure 1A). FACS analysis at 48 hours after B19 infection revealed 2 types of staining patterns for B19 protein following immunohistochemistry using PAR3: (1) intense staining in KU812Ep6 and (2) weak staining in Ku812Ep6, U937, H9, and ACHN (left column in Figure 1B). Replication of B19 DNA and the synthesis of B19 protein was observed in KU812Ep6, but not in any of the other cells, irrespective of the presence of P antigen (right column in Figure 1A and right column in Figure 1B) or α5β1 integrin.

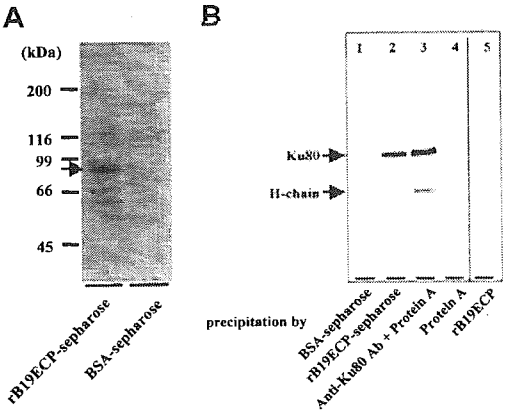


**Figure 2. Determination of B19-binding protein on surface of T cell line H9.** (A) Isolation of B19-binding protein from H9 surface. Surface proteins H9 of cells were biotinylated. Cell lysate from $1 \times 10^{11}$ biotinylated H9 cells was mixed with rB19ECP-conjugated Sepharose or with BSA-conjugated Sepharose. Precipitated protein was isolated and reacted with streptavidin–horseradish-peroxidase conjugate on PVDF membranes, followed by the chemiluminescence detection. (B) Western blotting of protein from H9 surface with anti-Ku80 antibody. Lanes 1-4 show cell lysate precipitated with indicated protein or protein-conjugated Sepharose. Lane 5 shows the rB19ECP (1 μg) resolved by electrophoresis under denaturing conditions.

To determine the cell-surface molecule responsible for B19 binding to H9 cells, a recombinant empty capsid protein of B19 (rB19ECP) was used. Biotinylated rB19ECP bound H9 in a dose-dependent manner (data not shown). We then purified the rB19ECP-binding molecule from the cell surface of H9 using rB19ECP-conjugated Sepharose (rB19ECP-Sepharose). The precipitated 80-kDa protein (Figure 2A) was analyzed by matrix-assisted laser desorption ionization-time of flight mass spectrometry. The obtained data were collated and submitted for homology search using the Swiss Prot and NCB Inr databases. The Ku80 autoantigen was identified as the gene product with the highest

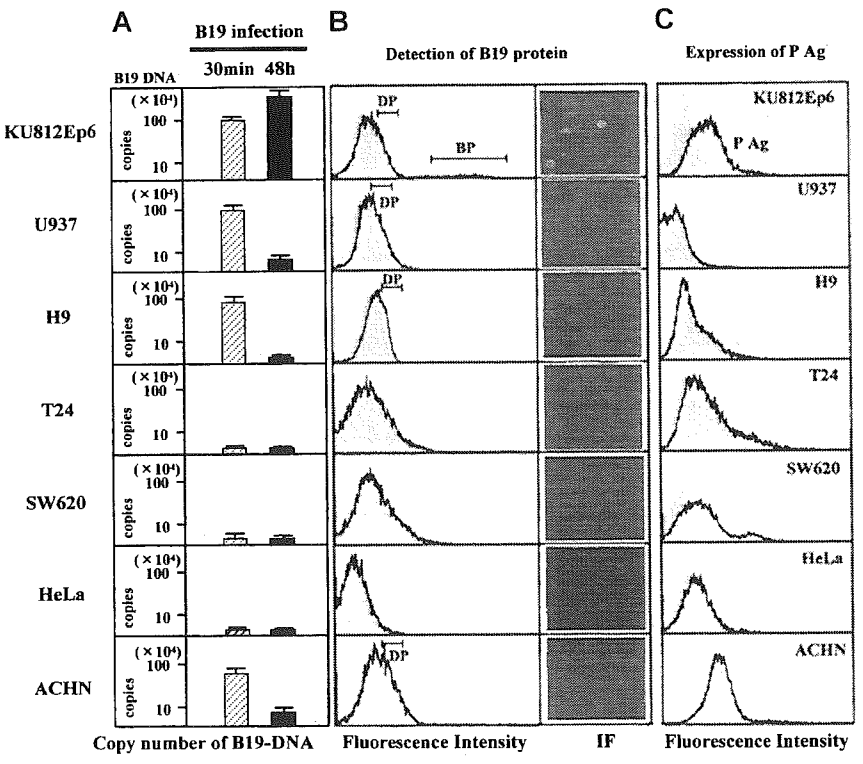


**Figure 1. B19 infectivity and expression of P antigen.** Each cell line ($2 \times 10^6$) was inoculated with B19 ($1 \times 10^{11}$ copies of B19 DNA) for 30 minutes at 4°C and washed with PBS, pH 7.2, 3 times. Half of the cells in each group were used for evaluation of B19 adsorption (left column in panel A), and remaining cells in 3 mL RPMI containing 10% FBS were further incubated at 37°C for 48 hours to measure B19 DNA replication (right column in panel A) or to detect B19 protein (B). (A) B19 binding and replication of B19 in various cell lines. B19-infected cells were quantified for B19 DNA as described in "Materials and methods." The left column (▨) is regarded as B19 adsorption, and the right column (■) as B19 replication. The scale for B19 DNA is shown in logarithm. (B) Detection of B19 protein in B19-infected cells. After a 48-hour incubation with B19, the cells were washed 3 times with PBS and they were fixed with 4% paraformaldehyde followed by permeabilization with SAP buffer (0.1% saponin, 0.05% $NaN_3$ in Hanks balanced salt solution). Then, cells were incubated with PAR3 at a concentration of 5 μg/mL on ice for 30 minutes, followed by an incubation with FITC-conjugated goat anti–mouse IgG. The expression of B19 protein in cytoplasm was analyzed by flow cytometry with PAR3 (line) or isotype-matched antibody 1F5 (shadow; left panel), or by immunofluorescence (IF) staining with PAR3 (right panel). Two types of positive patterns were observed in flow cytometry: dull positive (DP) pattern in KU812Ep6, U937, H9, and ACHN; bright positive (BP) pattern in KU812Ep6. (C) Flow cytometry analysis of P antigen expression on the cell surface. Indicated cells were incubated with antigloboside antibody, GL4, followed by PE-labeled anti–rabbit IgG. Shadow represents staining using rabbit IgG as a negative control.